Article

Structures of human pannexin 1 reveal ion pathways and mechanism of gating

https://doi.org/10.1038/s41586-020-2357-y

Received: 25 January 2020

Accepted: 3 April 2020

Published online: 3 June 2020

Check for updates

Zheng Ruan[1], Ian J. Orozco[1], Juan Du[1]✉ & Wei Lü[1]✉

Pannexin 1 (PANX1) is an ATP-permeable channel with critical roles in a variety of physiological functions such as blood pressure regulation[1], apoptotic cell clearance[2] and human oocyte development[3]. Here we present several structures of human PANX1 in a heptameric assembly at resolutions of up to 2.8 angström, including an apo state, a caspase-7-cleaved state and a carbenoxolone-bound state. We reveal a gating mechanism that involves two ion-conducting pathways. Under normal cellular conditions, the intracellular entry of the wide main pore is physically plugged by the C-terminal tail. Small anions are conducted through narrow tunnels in the intracellular domain. These tunnels connect to the main pore and are gated by a long linker between the N-terminal helix and the first transmembrane helix. During apoptosis, the C-terminal tail is cleaved by caspase, allowing the release of ATP through the main pore. We identified a carbenoxolone-binding site embraced by W74 in the extracellular entrance and a role for carbenoxolone as a channel blocker. We identified a gap-junction-like structure using a glycosylation-deficient mutant, N255A. Our studies provide a solid foundation for understanding the molecular mechanisms underlying the channel gating and inhibition of PANX1 and related large-pore channels.

Purinergic signalling has critical roles in diverse activities of the nervous system, including neuroprotection, synaptic transmission, nociception and inflammation[4–7]. Signalling is initiated by the release of ATP across the membrane by exocytosis[8] or through ATP-permeable channels[9–11]. The pannexin family is one such family of ATP-permeable channels and has three members in humans[12], PANX1, 2 and 3. PANX1 is widely expressed throughout the body and has crucial roles in physiological processes such as regulation of blood pressure, glucose uptake, inflammation and cell death[1,13–17]. Gain-of-function mutations in PANX1 are implicated in defects of oocyte development[3]. Thus, PANX1 has been considered a promising therapeutic target for many diseases. Compounds such as carbenoxolone (CBX) and trovafloxacin have previously been reported to inhibit the activity of PANX1[18,19]. However, little is known about where they bind or their mechanisms of inhibition.

PANXs are nonselective large-pored channels that share a four-transmembrane-domain arrangement with connexins, innexins, volume-regulated anion channels (VRACs), and calcium homeostasis modulators (CALHMs)[20–28]. Unlike connexins and innexins, PANXs are generally thought to not form gap junctions as a result of *N*-glycosylation[29–31], although one study has suggested that PANX1 may form gap junction in a cell-type-specific manner[32].

Under normal cellular conditions, PANX1 is autoinhibited by its C-terminal tail (CTT)[33,34]. However, it can be activated by membrane depolarization, extracellular potassium, intracellular calcium, tyrosine phosphorylation or mechanical stretching via unknown mechanisms[35–40]. Cleavage of the CTT, either during apoptosis or experimentally by caspase 3 or 7, also results in channel activation and ATP release[2,33].

To gain insight into the channel assembly, gating mechanism, ion conducting pathway and inhibitor binding site, we studied human PANX1 (hereafter, PANX1 refers to the human form unless specified otherwise) using a combination of single-particle cryo-electron microscopy (cryo-EM) and patch-clamp electrophysiology.

Overall structure

We determined structures of the wild-type human PANX1 (PANX1(WT)) in the presence of EDTA, Ca^{2+} or K^+. These structures are indistinguishable, suggesting that Ca^{2+} or K^+ is unlikely to directly activate PANX1. To study the location and role of the CTT and the N-terminal helix (NTH), we cleaved the CTT from the PANX1(WT) and from an NTH-truncation mutant using caspase 7, and determined their structures (PANX1(ΔCTT) and PANX1(ΔNTH/ΔCTT), respectively). We also determined structures of PANX1 bound to CBX (CBX–PANX1(ΔCTT) and CBX–PANX1(ΔNTH/ΔCTT)). To study the role of *N*-glycosylation of PANX1, we investigated the structure of a glycosylation-deficient mutant (N255A), which yielded both gap junctions (PANX1(N255A)^{Gap}) and hemichannels (PANX1(N255A)^{Hemi}). The structural determination is detailed in the Methods, and the results are summarized in Extended Data Tables 1–3. The structure of PANX1(ΔCTT) has the highest overall quality (map available at the Electron Microscopy Data Bank (EMD-21589) and model at the Protein Data Bank (6WBG)), and is therefore the reference structure for the discussion throughout the text unless otherwise noted.

The PANX1 channel forms a heptamer that contains (from top to bottom) an extracellular domain (ECD), a transmembrane domain (TMD) and an intracellular domain (ICD), with the unstructured CTT

[1]Van Andel Institute, Grand Rapids, MI, USA. ✉e-mail: juan.du@vai.org; wei.lu@vai.org

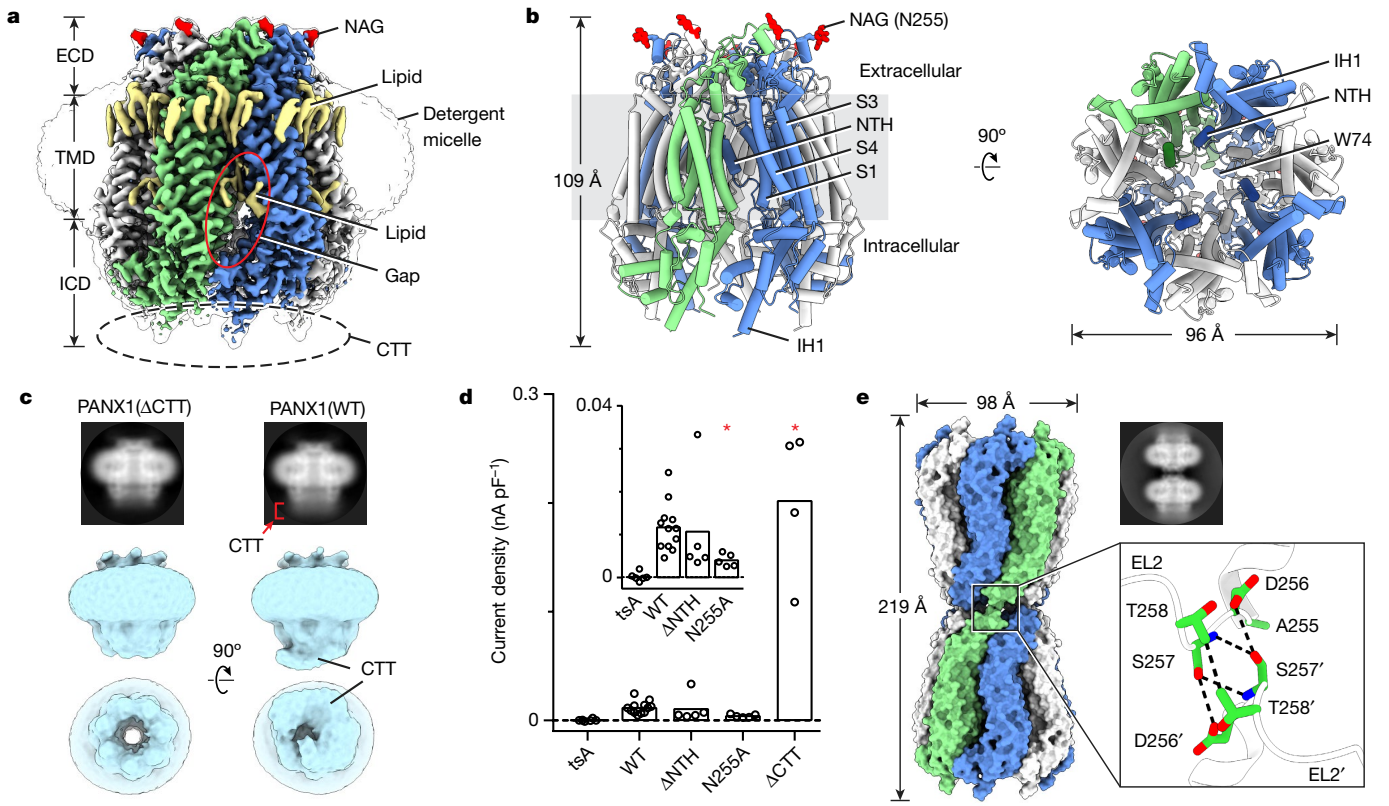

Fig. 1 | Overall architecture of PANX1. Odd- and even-numbered subunits are shown in blue and white, respectively; the seventh subunit is in green. **a**, The cryo-EM map of wild-type human PANX1 viewed parallel to the membrane. The unsharpened map is shown as a transparent envelope. Lipid-like densities and *N*-acetyl-D-glucosamine densities are shown in yellow and red, respectively. The position of the disordered CTT is outlined by a dashed ellipse. **b**, The structure of PANX1(WT); side (left) and bottom (right) views. **c**, The 2D class averages in side view, and the 3D classes obtained without imposing symmetry in both side and bottom views for PANX1(ΔCTT) and apo PANX(WT). The CTT densities in the 2D averages and 3D maps are labelled. **d**, Whole-cell CBX-sensitive current density (+80 mV, 5 ms) from patch-clamped tsA201 cells ($n = 6$ cells) and tsA201 cells overexpressing PANX1(WT) ($n = 12$) and mutants (ΔNTH, $n = 5$; N255A, $n = 5$; ΔCTT, $n = 4$). Each point represents one cell and the bar represents the mean. For statistical comparisons to wild type, a two-tailed unpaired Mann–Whitney test with Bonferroni correction was applied. $P = 0.748$ (ΔNTH), 0.011 (N255A) and 0.013 (ΔCTT). *$P < 0.05$. **e**, The structure and 2D class average (side view) of PANX1(N255A) gap junction shown in surface representation. The docking of two hemichannels is mediated through the EL2 linker, in which D256, S257 and T258 in the paired subunits form hydrophilic and hydrophobic interactions. ΔCTT and ΔNTH are deletion mutants that lack amino acids 2–20 and 380–426, respectively.

blocking the ICD entrance to the ion pathway along the symmetry axis (referred to as the main pore) (Fig. 1a, b). Caspase 7 treatment released the blockage by cleaving the CTT, opening the main pore (Fig. 1c). Removal of the CTT resulted in larger currents compared with the wild type (Fig. 1d, Extended Data Fig. 7a–c). The main pore narrows along the pore axis towards the extracellular side, with a small opening at the ECD entrance restricted by seven W74 residues.

In the TMD, four transmembrane helices (S1–S4) frame the exterior wall, and the NTH lines the interior wall in a domain-swapped manner—the NTH of one subunit interacts with the TMD of the adjacent subunit (Fig. 1b). Removal of the NTH yielded a TMD in a truncated elliptical-cone shape (Extended Data Figs. 2b, 6a, b), but still generated CBX-sensitive, voltage-dependent currents similar to those of the wild type (Fig. 1d, Extended Data Fig. 7a–c). We thus suggest a role for the NTH in maintaining a rigid TMD with a large pore.

While the ECD and the lower part of the ICD form close contacts between neighbouring subunits, there are gaps in the TMD and upper part of the ICD (Fig. 1a). The gap in the TMD is filled with lipid-like densities, similar to LRRC8A[25,26]. However, the gap in the upper ICD is solvent-exposed and connects to the main pore, implying the existence of an ion pathway. We also observed several strong lipid-like densities surrounding the upper part of the TMD, forming a lipid belt (Fig. 1a).

The gap junction PANX1(N255A)^{Gap} is formed by two hemichannels docked in a head-to-head manner solely through extracellular linker 2 (EL2) in the ECD (Fig. 1e, Extended Data Fig. 4c, d). This results in a substantially smaller contact area (122 Å^2 per paired subunit) than that of connexin 46 (942 Å^2) or innexin 6 (1,550 Å^2), in which both the EL1 and EL2 linkers participate in docking. The N255A mutant also forms a hemichannel and produces CBX-sensitive current (Fig. 1d, Extended Data Fig. 7a–c). Our results provide direct evidence that glycosylation is a key determinant of PANX1 gap junction formation, although it is worthwhile to note that the N255A gap junction structure may not represent a normal physiological conformation of the channel[41].

CBX blocks the extracellular entrance

In the CBX-bound structures, we observed a strong density at the extracellular entrance, which is surrounded by seven W74 residues (Fig. 2a–c). We assigned this density to CBX (although we were unable to unambiguously define its exact pose owing to structural heterogeneity) on the basis of several pieces of evidence. First, this density does not exist in the structures without CBX (Fig. 2c, Extended Data Figs. 2, 6). Second, the extracellular entrance provides an ideal chemical environment for the binding of CBX: the aromatic side chain of W74 interacts with the steroid-like core of CBX, the N terminus of helix EH1

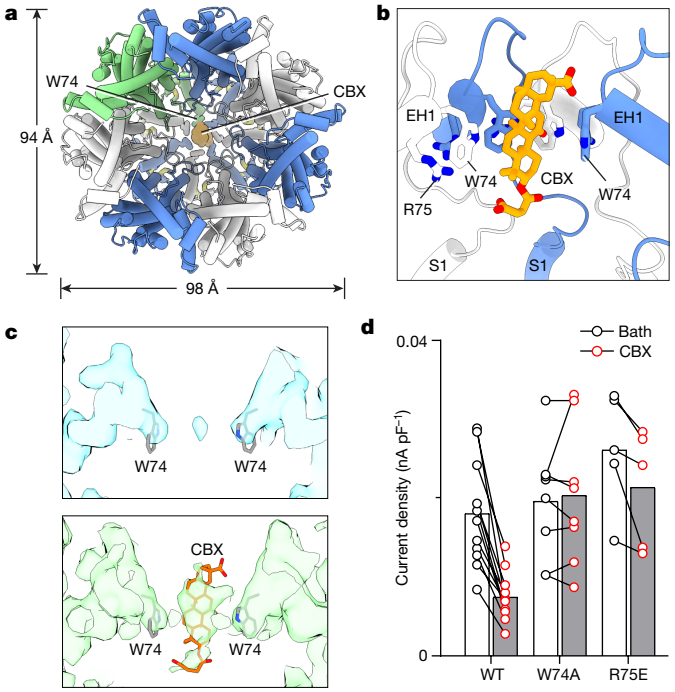

Fig. 2 | CBX binding site of PANX1. a, The structure of CBX–PANX1(ΔCTT) viewed from the intracellular side. **b**, The CBX binding site in the extracellular entrance. Alternate subunits are shown in blue and white. The three subunits in the front are hidden for clarity. **c**, Slice view of the extracellular entrance of PANX1(ΔCTT) and CBX–PANX1(ΔCTT) maps. The CBX and the side chain of W74 are shown in stick. **d**, Whole-cell current density (+80 mV, 5 ms) from patch-clamped tsA201 cells overexpressing PANX1(WT) ($n = 12$ cells), PANX1(W74A) ($n = 8$) or PANX1(R75E) ($n = 5$) before and after superfusion of extracellular solution containing 0.1 mM CBX. Each paired point represents an individual cell and the bar represents the mean. CBX inhibition for each construct was evaluated using a two-tailed paired Wilcoxon test with Bonferroni correction. $P = 0.0015$ (WT), 1.00 (W74A) and 0.18 (R75E).

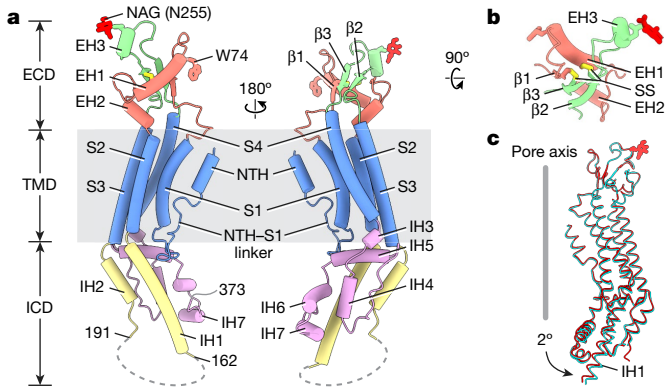

Fig. 3 | A single PANX1 subunit. a, The disordered IH1–IH2 linker (residues 163–190) and the CTT (residues after 373) are indicated by dashed lines. **b**, The ECD of a single subunit viewed from the extracellular side. SS, disulfide bond. **c**, Superposition of the subunits of PANX1(WT) (red) and PANX1(N255A) (cyan) aligned by the ECD.

and the side-chain of R75 provide favourable electrostatic potential to accommodate the two terminal carboxyl groups of CBX, and CBX is the right size to fit in the extracellular entrance. Third, the W74A and R75E mutations abolished and reduced CBX-dependent PANX1 inhibition[18,42], respectively (Fig. 2d, Extended Data Fig. 7a, c). A recent study also showed that the inhibition by CBX is markedly reduced in the R75A mutant of *Xenopus tropicalis* PANX1[43]. Finally, this binding site is supported by the loss of symmetry of the structure—the asymmetric CBX overlaps with the symmetry axis, breaking the C7 symmetry (Fig. 2a, Extended Data Fig. 2b). Together, our data support pore blocking as the mechanism of CBX inhibition of PANX1.

Single subunit

Each PANX1 protomer consists of a TMD connecting the ECD and ICD (Fig. 3a). The ECD is formed by two extracellular linkers, EL1 and EL2, mainly through two types of interaction. The β1 strand in EL1 forms an intact sheet with the β2 and β3 strands in EL2, and this interaction is strengthened by two disulfide bonds, one connecting β1 and β3 and the other connecting helix EH1 and β2 (Fig. 3b). Helix EH1 makes an angle of approximately 45° with the membrane and is the major component that forms the extracellular entrance with its W74 residue. N255A—at the top of the ECD in helix EH3—is glycosylated, preventing two hemichannels from docking into a gap junction (Fig. 3a, b, Extended Data Fig. 1g). The N255A mutation causes a subtle change in EH3 and a conformational rearrangement in the ICD characterized by an outward shift in the intracellular helix IH1 (Fig. 3c), which results in an expansion of the ICD (diameters of 96 and 98 Å, respectively; Fig. 1b, e).

The TMD consists of the short NTH and a tight helix bundle formed by S1–S4 (Fig. 3a). The NTH of PANX1 is unique among the large-pore channels because of its location. It spans the extracellular half of the TMD and, as a result, connects to S1 through a long and flexible linker (NTH–S1 linker); both the NTH and the linker line the main pore. By contrast, the NTH in connexins and innexins spans the intracellular half of the TMD and is connected to S1 by a short linker. The NTH in VRACs is only partially visible in the structure and runs along the intracellular face of the membrane[23–26]. Notably, in *X. tropicalis* PANX1, the NTH and NTH–S1 linker are positioned on the intracellular side but not within the TMD[42,43]. S1–S4 of PANX1 are arranged in an anticlockwise manner as viewed from intracellular side, with S1 tightly clamped between S2 and S4. This is the same arrangement as in connexins, innexins and VRAC, but it is distinct from that of CALHM2, in which S1–S4 are arranged clockwise and S1 is loosely attached to S3 (Extended Data Fig. 8).

The ICD is a helix-rich structure formed by the linker connecting S2 and S3 and the residues after S4 (Fig. 3a). Helix IH1 is long, extending deeply into the intracellular space as an extension of S2; it constitutes the main body of the ICD and is surrounded by six short helices. The long IH1 is reminiscent of the long cytoplasmic helix CH1 of CALHM2, but they have different structural roles. In PANX1, IH1 makes an angle of approximately 60° with the membrane and is not involved in intersubunit interactions, whereas in CALHM2, CH1 is nearly parallel to the membrane and participates extensively in intersubunit interactions[27,28]. The CTT is located downstream of IH7, the last intracellular helix, immediately after the caspase cleavage site. Although we were unable to model the CTT owing to its intrinsically disordered nature, we have defined its key role in caspase-dependent channel gating (see 'Ion pathways and channel gating').

Channel assembly

PANX1 is assembled through extensive interactions between the adjacent ECDs and between the adjacent lower ICDs, whereas the TMDs and upper ICD barely form contacts, creating a shallow crevice (Fig. 4a). Whereas the crevice in the TMD is occupied by lipids, the one in the ICD is solvent-exposed, resulting in a tunnel towards the main pore.

The ECD of PANX1 has a contact area of 1,069 Å^2 between adjacent subunits, which is larger than that of VRAC (936 Å^2), innexin (889 Å^2), connexin (342 Å^2) and CALHM2 (57 Å^2). The most distinctive feature is the seven W74 residues forming a ring in the centre of the pore and

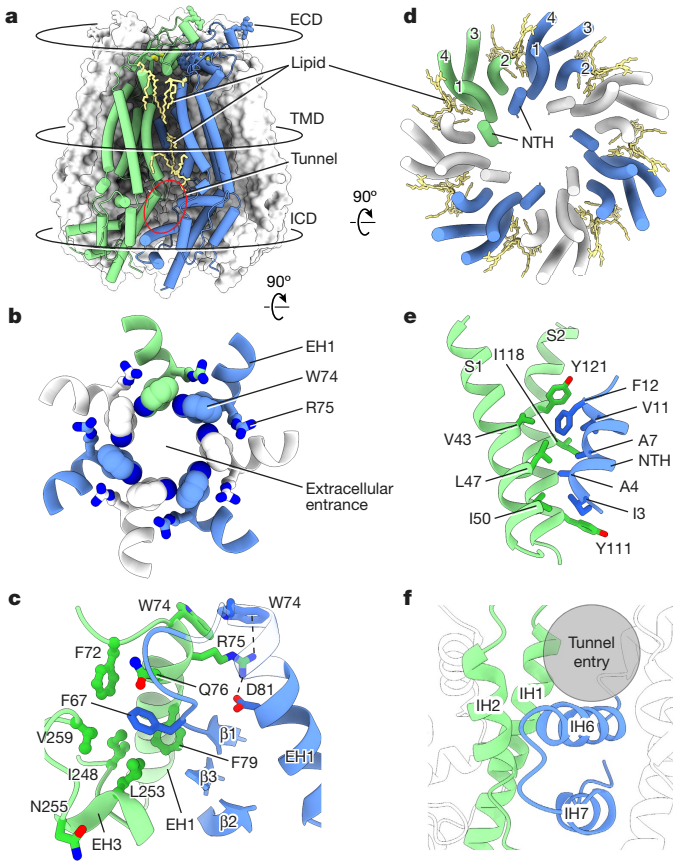

Fig. 4 | Channel assembly of PANX1. a, An overview of the intersubunit interfaces at the ECD, TMD and ICD using the wild-type PANX1 model. **b**, The intersubunit interface at the ECD, viewed from the intracellular side. The extracellular entrance is formed by W74 on the EH1 helix. **c**, The ECD intersubunit interface viewed parallel to the membrane. R75 forms a cation–π interaction and a salt bridge with the adjacent W74 and D81, respectively; F67 is inserted into a hydrophobic pocket in the adjacent subunit. Part of the EH1 is shown as transparent. **d**, The intersubunit interface of the TMD between NTH and the adjacent S1 and S2, viewed from the intracellular side. Only TMD helices are shown. The gap between adjacent TMDs is filled with lipids. **e**, The TMD interface viewed parallel to the membrane. **f**, The intersubunit interface at the lower part of the ICD between the IH1 and IH2 helices and the adjacent IH6 and IH7 helices. A crevice in the upper part of the ICD forms a tunnel that connects to the main pore.

the extracellular entrance (Fig. 4b), with the Nε1 atom of the Trp pyrrole ring pointing to the benzene ring in the adjacent residue. This entrance is encircled by a second layer of interaction, in which R75 is sandwiched between W74 and D81 of the adjacent helix EH1, forming a cation–π interaction and a salt bridge, respectively (Fig. 4c). These two layers of interaction form a rigid extracellular entrance containing positive charges. W74R or R75D/E mutations decreased the stability of PANX1 (Extended Data Fig. 1h–j), suggesting an important role of the cation–π interaction and salt bridge in channel assembly. The radius of the extracellular entrance is 4.4 Å, which is about the size of an ATP molecule. In addition to EH1, a β-sheet tightly organizes the close contact between adjacent ECDs (Fig. 4c). Specifically, in the centre of the ECD, F67 is inserted into a hydrophobic pocket formed by helices EH1 and EH3 of the neighbouring subunit. On the peripheral side of the ECD, strands β2 and β3 form multiple hydrophilic interactions with the EH3 of the adjacent subunit.

The TMD of PANX1 has a two-layer architecture; the helix bundle S1–S4 forms the exterior, and the NTH lines the ion-conducting pore (Fig. 4d). The NTH is clamped between the adjacent S1 and S2 in a domain-swapped manner, creating the only interactions between neighbouring TMDs (Fig. 4e). This domain-swapped interaction in the TMD is not present in connexin, innexin or VRAC (Extended Data Fig. 8).

The interface in the ICD is restricted to its lower part, where helices IH1 and IH2 interact with helices IH6 and IH7 from the adjacent subunit through hydrophobic and hydrophilic interactions (Fig. 4f). By contrast, the upper part of the ICD lacks interfaces and contains several positively charged residues, resulting in a tunnel between adjacent ICDs that is favourable for anions such as chloride but is not large enough for small molecules such as ATP.

Ion pathways and channel gating

To understand how PANX1 gates under different physiological conditions, we investigated potential ion-conducting pathways in the structures other than the main pore along the symmetry axis. We found strong evidence that the seven side tunnels in the upper ICD (Fig. 5a, c) serve as an alternative pathway for conducting ions, and we have thus established a gating mechanism involving the two pathways by combining data from cryo-EM, patch-clamp electrophysiology and molecular dynamics simulation.

The main pore is in the shape of a truncated cone. Both the extracellular and intracellular entrances are positively charged (Fig. 5b, d), making the pore favourable for negatively charged cargos such as chloride and ATP. The extracellular entrance is constricted by seven W74–R75 residue pairs in a rigid conformation. We investigated the functional importance of these residues by performing electrophysiological experiments. While the W74A mutant remained voltage-dependent similar to the wild type, its anion selectivity was altered, resulting in equal permeability of iodide and chloride—in contrast to the wild type, which shows a preference for iodide over chloride[44] (Extended Data Fig. 7a, b, d–f). Moreover, a charge-reversing mutant, R75E, showed a loss of voltage dependence and anion selectivity and a marked increase in permeability of sodium over chloride (Extended Data Fig. 7a, b, d–f). We therefore suggest that the extracellular constriction site has a role in discriminating cargoes on the basis of their charge and size, but it is unlikely to act as a gate that alters its conformation during channel opening and closing. This is in agreement with a recent study in which mutants of the extracellular entrance in *X. tropicalis* PANX1 also affect ion selectivity[42].

Although the NTH lines the main pore within the TMD, it probably does not act as a gate either, because it is clamped by the adjacent S1 and S2 and thus lacks the flexibility to close the pore. Indeed, an NTH-deletion construct produced CBX-sensitive conductance similar to that of the wild type (Fig. 1d, Extended Data Fig. 7a–c). Instead, we observed that the intracellular entry was blocked by the unstructured CTT, and this blockage was released upon removal of the CTT by caspase 7, opening the main pore (Fig. 1c). Although it has been proposed that the autoinhibitory CTT is cleaved by caspase 3 or caspase 7 to open the channel during apoptosis[2,33,34], our study provided a first visualization of such a gating mechanism, supporting the idea that the main pore is gated by CTT in a caspase-dependent manner.

This leads to the question of how PANX1 is gated under normal (nonapoptotic) conditions, given that it produces a small but measurable ionic conductance in the absence of caspase treatment[33,35] (Fig. 5f, Extended Data Fig. 7a–c). The seven tunnels at the ICD intersubunit interface may have a role in this gating. These tunnels contain several positively charged residues and other polar residues, which make them accessible to solvent and anions (Fig. 5a–d). The peripheral part of the tunnel, surrounded by S1 and IH5, and S2 and IH1 of adjacent subunits, is wide enough to accommodate fully hydrated chloride ions (Fig. 5d). The tunnel gradually narrows towards the interior, which is formed by the adjacent NTH–S1 linkers. Notably, deletions (the Δ21–23 disease mutant[3] and Δ21–27) on this linker result in a gain-of-function phenotype (Fig. 5a, f, Extended Data Fig. 7a–c). We therefore propose that the

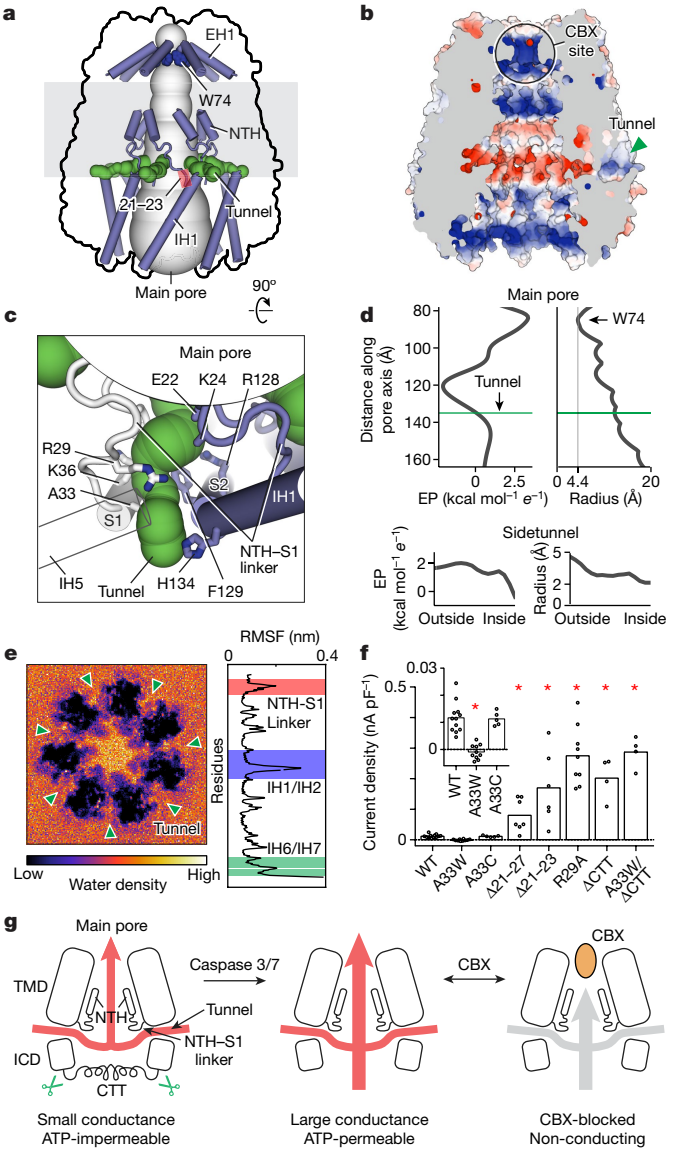

Fig. 5 | Ion-conducting pathways and channel gating. a, An overview of the main pore (grey body) and the side tunnels (green) in PANX1. The structural elements lining the pore are shown as cartoons. The position of the disease-causing, gain-of-function mutation in the NTH–S1 linker (Δ21–23) is highlighted by a red box. **b**, The interior surface of PANX1 coloured according to the electrostatic surface potential from −3 to +3 kT e^{-1} (red to blue). **c**, The key elements that constitute the side tunnel. IH5 is shown as a transparent tube for clarity. **d**, The size and electrostatic potential (EP) profiles of the main pore and side tunnel. In the top panel, the *y*-axis is numbered according to PDB coordinates along the *z* dimension; the locations of the side tunnel and W74 are marked. **e**, Molecular dynamics simulation of PANX1. Left, density of water molecules projected using a range of 127.6–145.6 Å along the *z* dimension (PDB coordinates) covering the side tunnel. Right, average root mean square fluctuation (RMSF) of single PANX1-subunit C_α atoms from a 100-ns molecular dynamics trajectory. The NTH–S1 linker (red), IH1 and IH2 (blue), and IH6 and IH7 (green) showed the highest flexibility; the NTH–S1 linker gates the tunnel, whereas IH1, IH2, IH6 and IH7 constitute the periphery of the tunnel. **f**, Whole-cell CBX-sensitive current density (+80 mV, 5 ms) from patch-clamped tsA201 cells overexpressing PANX1(WT) ($n = 12$), PANX1(A33W) ($n = 10$), PANX1(A33C) ($n = 5$), PANX1(Δ21–27) ($n = 7$), PANX1(Δ21–23) ($n = 6$), PANX1(R29A) ($n = 9$), PANX1(ΔCTT) ($n = 4$) or PANX1(A33W/ΔCTT) ($n = 4$). For statistical comparisons to wild type, a two-tailed Mann–Whitney test with Bonferroni correction was applied. $P = 0.0006$ (A33W), 1.00 (A33C), 0.011 (Δ21–27), 0.006 (Δ21–23), 0.003 (R29A), 0.031 (ΔCTT) and 0.031 (A33W/CTT). *$P < 0.05$. **g**, Cartoon showing the two ion pathways and the mechanism of CBX blocking.

NTH–S1 linker may act as a gate, and its shortening may result in less blockage of the tunnel. Within the tunnel, we identified two constriction sites formed by R29 and A33 on the NTH–S1 linker, with radii of 2.9 and 2.0 Å, respectively, suggesting that partial dehydration is probably required for chloride ions to pass through the tunnel.

To investigate whether the side tunnel is indeed an alternative ion-conducting pathway and the flexible NTH-S1 linker functions as a gate, we performed molecular dynamics simulations and electrophysiology experiments. Simulations showed that this tunnel was hydrated and that the NTH–S1 linker had high flexibility (Fig. 5e). Next, we mutated the two constriction residues, R29A and A33W, aiming to enlarge and shrink the tunnel, respectively. As expected, the R29A mutant yielded approximately 30-fold-higher CBX-sensitive current relative to the wild type, but the A33W mutation completely abolished CBX-sensitive current (Fig. 5f, Extended Data Fig. 7a–c). By contrast, truncating the CTT from the A33W mutant generated large currents comparable to the PANX1(ΔCTT), indicating that the side tunnel and the main pore are gated independently (Fig. 5f). As a control, mutating A33 to a residue of similar size, Cys, did not alter the channel function (Fig. 5f). Together, our structural and functional data strongly support the idea that the tunnels constitute an alternative ion pathway that is gated by the NTH–S1 linker and operates independently from the CTT. We found that innexin and VRAC also contain side tunnels; thus, side tunnels may be a common feature of these large-pore channels.

Discussion

Our studies on PANX1 addressed longstanding questions regarding its channel architecture, gap junction formation, ligand-binding site, ion pathways and mechanisms of channel gating and inhibition. Our structures support a previous study suggesting that the linker connecting helix S1 and strand β1 (residues I60, G61 and T62) lines the channel pore[45]. We have identified two ion-conducting pathways—the main pore along the symmetry axis, and seven side tunnels in the ICD (Fig. 5g). Under normal physiological conditions, the intracellular entrance of the main pore is blocked by the unstructured CTT, so anions—but not ATP—can move through the side tunnels, which explains why PANX1 currents can be evoked with a voltage clamp, during which there is no ATP release[36,46]. During apoptosis, the CTT is cleaved by caspase, which opens the main pore for the release of ATP, triggering signals that attract phagocytes to engulf the dying cells. Both pathways can be blocked by CBX because it occupies the entrance at the extracellular side.

Notably, PANX1 has previously been reported to release ATP or open into a high-conductance state as a result of phosphorylation of tyrosine residues[38,39]. In our structures, these tyrosine residues are located in the lower portion of the ICD, suggesting that their phosphorylation may regulate the conformation of the nearby CTT. Further studies are required to fully understand the phosphorylation-dependent activation mechanism.

Online content

Any methods, additional references, Nature Research reporting summaries, source data, extended data, supplementary information, acknowledgements, peer review information; details of author contributions and competing interests; and statements of data and code availability are available at https://doi.org/10.1038/s41586-020-2357-y.

1. Billaud, M. et al. A molecular signature in the pannexin1 intracellular loop confers channel activation by the α1 adrenoreceptor in smooth muscle cells. *Sci. Signal.* **8**, ra17 (2015).
2. Chekeni, F. B. et al. Pannexin 1 channels mediate 'find-me' signal release and membrane permeability during apoptosis. *Nature* **467**, 863–867 (2010).
3. Sang, Q. et al. A pannexin 1 channelopathy causes human oocyte death. *Sci. Transl. Med.* **11**, eaav8731 (2019).
4. Tozaki-Saitoh, H., Tsuda, M. & Inoue, K. Role of purinergic receptors in CNS function and neuroprotection. *Adv. Pharmacol.* **61**, 495–528 (2011).

5. Ren, J. & Bertrand, P. P. Purinergic receptors and synaptic transmission in enteric neurons. *Purinergic Signal.* **4**, 255–266 (2008).
6. Tsuda, M., Tozaki-Saitoh, H. & Inoue, K. Pain and purinergic signaling. *Brain Res. Rev.* **63**, 222–232 (2010).
7. Le, T.-T. T. et al. Purinergic signaling in pulmonary inflammation. *Front. Immunol.* **10**, 1633 (2019).
8. Zhang, Z. et al. Regulated ATP release from astrocytes through lysosome exocytosis. *Nat. Cell Biol.* **9**, 945–953 (2007).
9. Dahl, G. ATP release through pannexon channels. *Phil. Trans. R. Soc. Lond. B* **370**, 20140191 (2015).
10. Taruno, A. et al. CALHM1 ion channel mediates purinergic neurotransmission of sweet, bitter and umami tastes. *Nature* **495**, 223–226 (2013).
11. Anselmi, F. et al. ATP release through connexin hemichannels and gap junction transfer of second messengers propagate Ca^{2+} signals across the inner ear. *Proc. Natl Acad. Sci. USA* **105**, 18770–18775 (2008).
12. Penuela, S., Gehi, R. & Laird, D. W. The biochemistry and function of pannexin channels. *Biochim. Biophys. Acta* **1828**, 15–22 (2013).
13. Adamson, S. E. et al. Pannexin 1 is required for full activation of insulin-stimulated glucose uptake in adipocytes. *Mol. Metab.* **4**, 610–618 (2015).
14. Makarenkova, H. P., Shah, S. B. & Shestopalov, V. I. The two faces of pannexins: new roles in inflammation and repair. *J. Inflamm. Res.* **11**, 273–288 (2018).
15. Thompson, R. J. et al. Activation of pannexin-1 hemichannels augments aberrant bursting in the hippocampus. *Science* **322**, 1555–1559 (2008).
16. Silverman, W. R. et al. The pannexin 1 channel activates the inflammasome in neurons and astrocytes. *J. Biol. Chem.* **284**, 18143–18151 (2009).
17. Crespo Yanguas, S. et al. Pannexin1 as mediator of inflammation and cell death. *Biochim. Biophys. Acta* **1864**, 51–61 (2017).
18. Michalski, K. & Kawate, T. Carbenoxolone inhibits pannexin1 channels through interactions in the first extracellular loop. *J. Gen. Physiol.* **147**, 165–174 (2016).
19. Poon, I. K. H. et al. Unexpected link between an antibiotic, pannexin channels and apoptosis. *Nature* **507**, 329–334 (2014).
20. Myers, J. B. et al. Structure of native lens connexin 46/50 intercellular channels by cryo-EM. *Nature* **564**, 372–377 (2018).
21. Maeda, S. et al. Structure of the connexin 26 gap junction channel at 3.5 Å resolution. *Nature* **458**, 597–602 (2009).
22. Oshima, A., Tani, K. & Fujiyoshi, Y. Atomic structure of the innexin-6 gap junction channel determined by cryo-EM. *Nat. Commun.* **7**, 13681 (2016).
23. Kefauver, J. M. et al. Structure of the human volume regulated anion channel. *eLife* **7**, e38461 (2018).
24. Kasuya, G. et al. Cryo-EM structures of the human volume-regulated anion channel LRRC8. *Nat. Struct. Mol. Biol.* **25**, 797–804 (2018).
25. Deneka, D., Sawicka, M., Lam, A. K. M., Paulino, C. & Dutzler, R. Structure of a volume-regulated anion channel of the LRRC8 family. *Nature* **558**, 254–259 (2018).
26. Kern, D. M., Oh, S., Hite, R. K. & Brohawn, S. G. Cryo-EM structures of the DCPIB-inhibited volume-regulated anion channel LRRC8A in lipid nanodiscs. *eLife* **8**, e42636 (2019).
27. Choi, W., Clemente, N., Sun, W., Du, J. & Lü, W. The structures and gating mechanism of human calcium homeostasis modulator 2. *Nature* **576**, 163–167 (2019).
28. Syrjanen, J. L. et al. Structure and assembly of calcium homeostasis modulator proteins. *Nat. Struct. Mol. Biol.* **27**, 150–159 (2020).
29. Sosinsky, G. E. et al. Pannexin channels are not gap junction hemichannels. *Channels (Austin)* **5**, 193–197 (2011).
30. Boassa, D. et al. Pannexin1 channels contain a glycosylation site that targets the hexamer to the plasma membrane. *J. Biol. Chem.* **282**, 31733–31743 (2007).
31. Beckmann, A., Grissmer, A., Krause, E., Tschernig, T. & Meier, C. Pannexin-1 channels show distinct morphology and no gap junction characteristics in mammalian cells. *Cell Tissue Res.* **363**, 751–763 (2016).
32. Sahu, G., Sukumaran, S. & Bera, A. K. Pannexins form gap junctions with electrophysiological and pharmacological properties distinct from connexins. *Sci. Rep.* **4**, 4955 (2014).
33. Sandilos, J. K. et al. Pannexin 1, an ATP release channel, is activated by caspase cleavage of its pore-associated C-terminal autoinhibitory region. *J. Biol. Chem.* **287**, 11303–11311 (2012).
34. Chiu, Y.-H. et al. A quantized mechanism for activation of pannexin channels. *Nat. Commun.* **8**, 14324 (2017).
35. Michalski, K., Henze, E., Nguyen, P., Lynch, P. & Kawate, T. The weak voltage dependence of pannexin 1 channels can be tuned by N-terminal modifications. *J. Gen. Physiol.* **150**, 1758–1768 (2018).
36. Wang, J. et al. The membrane protein pannexin1 forms two open-channel conformations depending on the mode of activation. *Sci. Signal.* **7**, ra69 (2014).
37. Locovei, S., Wang, J. & Dahl, G. Activation of pannexin 1 channels by ATP through P2Y receptors and by cytoplasmic calcium. *FEBS Lett.* **580**, 239–244 (2006).
38. DeLalio, L. J. et al. Constitutive SRC-mediated phosphorylation of pannexin 1 at tyrosine 198 occurs at the plasma membrane. *J. Biol. Chem.* **294**, 6940–6956 (2019).
39. Weilinger, N. L. et al. Metabotropic NMDA receptor signaling couples Src family kinases to pannexin-1 during excitotoxicity. *Nat. Neurosci.* **19**, 432–442 (2016).
40. Furlow, P. W. et al. Mechanosensitive pannexin-1 channels mediate microvascular metastatic cell survival. *Nat. Cell Biol.* **17**, 943–952 (2015).
41. Penuela, S., Celetti, S. J., Bhalla, R., Shao, Q. & Laird, D. W. Diverse subcellular distribution profiles of pannexin 1 and pannexin 3. *Cell Commun. Adhes.* **15**, 133–142 (2008).
42. Michalski, K. et al. The cryo-EM structure of pannexin 1 reveals unique motifs for ion selection and inhibition. *eLife* **9**, e54670 (2020).
43. Deng, Z. et al. Cryo-EM structures of the ATP release channel pannexin 1. Preprint at https://www.biorxiv.org/content/10.1101/2020.01.05.895235v1 (2020).
44. Ma, W. et al. Pannexin 1 forms an anion-selective channel. *Pflugers Arch.* **463**, 585–592 (2012).
45. Wang, J. & Dahl, G. SCAM analysis of Panx1 suggests a peculiar pore structure. *J. Gen. Physiol.* **136**, 515–527 (2010).
46. Romanov, R. A. et al. The ATP permeability of pannexin 1 channels in a heterologous system and in mammalian taste cells is dispensable. *J. Cell Sci.* **125**, 5514–5523 (2012).

Methods

No statistical methods were used to predetermine sample size. The experiments were not randomized. The investigators were not blinded to allocation during experiments and outcome assessment.

Constructs and cloning

Full-length human PANX1 (UniprotID: Q96RD7) was synthesized by GenScript and subcloned into a pEG Bacmam vector between XbaI and NotI restriction sites[47]. The C-terminal end of the translated product contains a thrombin digestion site (Leu-Val-Pro-Arg-ll-Gly-Ser), an enhanced green fluorescent protein (eGFP), a StrepII tag and a 8× His tag. Caspase 3 and caspase 7 plasmids were obtained from Addgene (plasmids 11821 and 11825)[48]. Primers for site-directed mutagenesis were designed using NEBaseChanger (https://nebasechanger.neb.com/) and synthesized by Eurofins Genomics. The Q5 site-directed mutagenesis protocol was used to generate all the mutants (ΔNTH, W74A, N255A, Δ21-23, R29A, A33W, A33W/ΔCTT, ΔCTT and A33C). ΔNTH represents a PANX1 mutant in which residues 2–20 were deleted. ΔCTT corresponds to a G380* (stop codon) mutation to mimic the caspase-cleaved PANX1. Positive clones were confirmed by Sanger sequencing from Eurofins Genomics.

Transfection and solubilization test

The Sf9 and tsA201 cells used in this study were purchased from ATCC; the cells were routinely maintained in our laboratory; they were not authenticated; they tested negative for mycoplasma contamination. Adherent tsA201 cells were grown at 37 °C in DMEM medium with 10% FBS. Cells were transfected using Lipofectamine 2000 following the manufacturer's protocol. The next day, sodium butyrate was added to 10 mM and the cells were incubated at 30 °C. After 24 h, cells were collected and stored at −80 °C. For fluorescence size-exclusion chromatography (FSEC), cells were solubilized using 500 µl of 150 mM NaCl, 20 mM Tris-HCl pH 8.0 (TBS) buffer with 1% glyco-diosgenin (GDN) or SMA30010 for 1 h at 4 °C. The solubilized sample was clarified by ultracentrifugation at 87,000*g* and analysed by high-performance liquid chromatography. The supernatant (20 µl) was injected onto a Superose 6 Increase 5/150 GL column (GE Healthcare) at a flow rate of 0.3 ml min^{-1}. GFP (480 nm) and tryptophan (280 nm) absorbance were monitored to determine protein solubility and retention volume.

Deglycosylation test

Adherent tsA201 cells infected with eGFP-tagged PANX1 or PANX1(N255A) were solubilized using 100 µl TBS buffer with 1% GDN at 4 °C for 1 h. The samples were then centrifuged at 20,000*g* for 30 min. The supernatant (16 µl) was mixed with 2 µl of GlycoBuffer 2 and 2 µl PNGase F enzyme. The control reaction was made by adding 2 µl of water instead of PNGase F enzyme. After overnight incubation at room temperature, the sample was mixed with 10 µl 2× SDS loading buffer (with 5% β-mercaptoethanol) and resolved by SDS–PAGE. GFP signal and far red signal (Alexa 488 and Alexa 680) of the gel was detected and merged using the ChemiDoc imaging system.

Protein expression and purification

Caspase 3 and 7 protein was expressed in *Escherichia coli* BL21 (NEB) and purified using a protocol established previously[49]. For PANX1 protein, a mammalian cell expression system optimized for membrane ion channel proteins was used[50]. Specifically, bacmid was produced by transforming pEG-PANX1 plasmid into DH10α cells. Positive colonies were selected from a LB plate (Teknova) with 50 µg ml^{-1} kanamycin, 10 µg ml^{-1} tetracycline, 7 µg ml^{-1} gentamicin, 40 µg ml^{-1} IPTG and 100 µg ml^{-1} Bluo-gal. Bacmid from positive clones was extracted and transfected into adherent Sf9 cells using Cellfectin II reagent using the manufacturer's protocol. Five days after transfection, P1 virus was filtered and collected. P2 virus was produced by infecting suspension Sf9 cells at 0.9×10^6 cells per ml in a 5,000:1 v/v ratio. Five days after infection, P2 virus was collected and supplemented with 2% FBS. P2 virus was stored at 4 °C and protected from light.

Suspension tsA201 cells were grown at 37 °C in FreeStyle 293 medium supplemented with 1% FBS. The cells were infected with 5% v/v P2 virus at a density of 3.5×10^5 cells per ml and grown at 37 °C. Twelve hours after infection, sodium butyrate was added to a final concentration of 5 mM and cells were grown at 30 °C. Cells were collected 56 h after infection and stored at −80 °C until further use.

Infected tsA201 cells expressing PANX1(200 ml culture) were thawed on ice and suspended with TBS buffer. Cells were then solubilized with 1% GDN and a protease inhibitor cocktail (1 mM PMSF, 0.8 µM aprotinin, 2 µg ml^{-1} leupeptin and 2 mM pepstatin A) for 1 h at 4 °C. The sample was clarified by centrifugation at 5,000*g* for 15 min and ultracentrifugation at 186,000*g* for 1 h. The supernatant was mixed with 2.5 ml Talon resin using a batch protocol. Imidazole (10 mM) was added to the sample to prevent nonspecific binding. After 1 h, the resin was washed using 2 × 10ml TBS buffer with 0.01% GDN and 20 mM imidazole. Protein was eluted with 4× TBS buffer with 0.01% GDN and 250 mM imidazole. The eluent was concentrated to 500 µl using a 100-kDa concentrator (Millipore). The C-terminal GFP was cleaved by thrombin (0.005 mg ml^{-1}) or caspase 7 (0.02 mg ml^{-1}). GFP-cleaved protein was further purified by size-exclusion chromatography (SEC) using a Superose 6 Increase 10/300 GL column (GE Healthcare) with TBS buffer containing 0.01% GDN as the mobile phase. Peak fractions were concentrated to 4–8 mg ml^{-1} for grid freezing.

For PANX1 protein purification using styrene-maleic acid copolymer (SMA), 200 ml of thawed tsA201 cells were initially solubilized in 20 ml TBS buffer with 1% SMA30010 at 4 °C. After 2 h, the sample was diluted to 50 ml using TBS buffer, followed by 2 rounds of ultracentrifugation at 186,000*g* for 1 h each. The supernatant was then diluted to 150 ml final volume using TBS buffer and applied to 7.5 ml Talon resin to allow batch binding at 4 °C overnight. The resin was washed with 60 ml TBS buffer containing 10 mM imidazole. Protein was eluted with 22.5 ml TBS buffer containing 250 mM imidazole and concentrated to 500 µl using a 100-kDa concentrator. The GFP tag was cleaved with thrombin (0.05 mg ml^{-1}) at room temperature for 4 h. GFP-free protein was further purified by SEC using TBS buffer. Peak fractions were concentrated to 7 mg ml^{-1} for grid freezing.

Cryo-EM sample preparation and data collection

Purified full-length PANX1 showed well-behaved biochemical properties in detergent or SMAs (Extended Data Fig. 1a–f). The PANX1 protein sample was first mixed with designated additives and ligand to the desired concentration before the grid freezing. Quantifoil 300 mesh 2/1 Au or Cu grids were glow discharged for 30 s. The protein (3 µl) was added to the grid in Vitrobot Mark III at 100% humidity. Grids were then blotted for 2 s, flash-frozen in liquid ethane, and stored in liquid nitrogen.

Preliminary grid screening was conducted using a 200-kV Talos Arctica microscope equipped with a Falcon III direct electron detection detector (FEI). High-resolution data collection was conducted using a 300-kV Talos Krios microscope equipped with a K2 Summit or K3 direct electron detector (Gatan). SerialEM was used to automate the data collection using a super-resolution counting mode[51]. The calibrated pixel size for the K2 and K3 cameras are 1.026 Å and 0.812 Å, respectively. For the K2 camera, the total exposure time is 8 s for 40 frames with a dose rate of 6.2 e^- $Å^{-2}$ s^{-1} for each micrograph. For the K3 camera, the exposure time is 1.5 s for 75 frames with a dose rate of 31.5 e^- $Å^{-2}$ s^{-1} for each micrograph. The nominal defocus range was specified from −1.2 µm to −1.9 µm with a 0.1-µm step. The raw movies were saved in LZW compressed .tif format for further processing.

Cryo-EM single-particle analysis

The data processing workflow and statistics are summarized in Extended Data Figs. 2, 5, and Extended Data Tables 1–3. Specifically,

raw movies were first motion-corrected using motioncor2 v.1.2.1 (ref. [52]). The contrast transfer function (CTF) of each micrograph was estimated using gctf v.1.06 or ctffind v.4.1.10 (refs. [53,54]). For K2 data, particle picking was performed using gautomatch (http://www.mrc-lmb.cam.ac.uk/kzhang/). For K3 data, Relion 3.0 was used for particle picking[55]. Junk particles were removed by two rounds of reference-free 2D classifications in Relion 3.0. The initial 3D model was generated using Cryosparc[56]. Particles were further cleaned by 3D classification. High-resolution classes with clear secondary structure features were used for 3D refinement. The initial refinement was conducted using C1 symmetry without a solvent mask. A solvent mask was then generated and used for subsequent 3D refinement jobs. The map is then checked manually to identify whether the structure adheres to C7 symmetry. CTF refinement and Bayesian polishing were also performed in Relion3.1b to further improve the refinement result[57,58].

For the PANX1(N255A) dataset, side and tilted views of the hemichannel particles and gap junction particles were separated during 2D classification. The top and down views of hemichannel and gap junction were difficult to separate from 2D class averages. We combined all top and down views with the hemichannel and gap junction dataset, and classified the particles using 3D classification (Extended Data Fig. 5). After a homogeneous particle set for hemichannel or gap junction was obtained, the map was refined using the same procedure as the other non-gap-junction datasets.

Structural determination

We focused on PANX1 in detergent because it yielded cryo-EM maps at substantially higher resolutions than PANX1 in SMA (Extended Data Tables 1–3). We first determined the PANX1 structures (Extended Data Figs. 2a, 3b–d) in the presence of 1 mM EDTA, 5 mM Ca^{2+} or 150 mM KCl, aiming to capture the apo, Ca^{2+}-activated and K^+-activated states, respectively. We also wanted to address the question of whether Ca^{2+} or K^+ directly activates PANX1 given the contradictory evidence in the literature[16,34,36,59–61]. All three structures formed only hemichannels having sevenfold symmetry. The heptameric stoichiometry was confirmed by the structure of SMA-extracted PANX1 (Extended Data Fig. 3a). Because no noticeable difference was observed among these three structures, we combined the data, yielding a structure with improved quality at 2.8 Å (PANX(WT)) (Fig. 1a, b, Extended Data Figs. 3e, 4a, b, Extended Data Table 1). Our structures suggest that it is unlikely that Ca^{2+} or K^+ directly activate human PANX1.

The CTT after the caspase cleavage site is predicted to be disordered[62]; it is not visible in the cryo-EM maps refined with C7 symmetry (Fig. 1a). However, we observed densities covering the intracellular entrance in the 3D class obtained without imposing symmetry (Fig. 1c). Because the location matches where the CTT was predicted to be according to functional studies[34], we determined the structure of PANX1 after cleaving the CTT using caspase 7 (PANX1(ΔCTT)) (Extended Data Table 2). Although the C7 refined structure of PANX1(ΔCTT) is identical to the full-length PANX1 structure, the densities blocking the intracellular entrance disappeared in the 3D class without imposing symmetry (Fig. 1c). We therefore concluded that these densities are indeed derived from the flexible CTT.

We observed extra density associated with the side chain of N255, indicating that this asparagine is glycosylated, which was confirmed by a deglycosylation assay (Extended Data Fig. 1g). PANX1 was thought to not form gap junctions owing to the *N*-glycosylation in its extracellular loop[30,31,63]. To provide a structural basis for this idea, we studied the structure of a glycosylation-deficient mutant N255A (Extended Data Fig. 5), which yielded both gap junctions (PANX1(N255A)^{Gap}) and hemichannels (PANX1(N255A)^{Hemi}) at an approximate ratio of 1:5 (grid concentration, about 23 μM) at resolutions of 2.83 and 2.86 Å, respectively (Extended Data Figs. 3j, 4c, d, Extended Data Table 3).

To study PANX1 inhibition, we determined the structure of the complex with CBX (CBX–PANX1(ΔCTT)). Because the structure showed obvious asymmetry and the CBX site overlapped with the symmetry axis, we refined the structure without imposing any symmetry to avoid symmetry-axis-associated noise or artefacts; the final resolution was 4.4 Å (Extended Data Fig. 3g, Extended Data Table 2). In addition to the change in overall structure, we noticed two differences between CBX–PANX1(ΔCTT) and the PANX1(ΔCTT) map. First, the centre of the extracellular restriction site (W74) is filled with strong density in the CBX–PANX1(ΔCTT) map, but not in the PANX1(ΔCTT) map. Second, the NTH density is weaker and seems to have been shifted in the CBX–PANX1(ΔCTT) map when compared to the PANX1(ΔCTT) map. We were initially not confident in assigning NTH to this density in the cryo-EM map of CBX–PANX1(ΔCTT). To resolve this uncertainty, we studied the structure of a PANX1 mutant in which residues 2–20 were deleted (ΔNTH mutant). Both PANX1(ΔNTH/ΔCTT) and CBX–PANX1(ΔNTH/ΔCTT) structures are non-symmetric and adopt an elliptical shape similar to CBX–PANX1(ΔCTT) (Extended Data Fig. 6a, b, Extended Data Table 2). In addition, the 'shifted' NTH density is not observed in either PANX1(ΔNTH/ΔCTT) or the CBX–PANX1(ΔNTH/ΔCTT) structure, suggesting that the shifted density in CBX–PANX1(ΔCTT) is indeed NTH. Additionally, we observed strong density located in the centre of the extracellular restriction site for CBX–PANX1(ΔNTH/ΔCTT), but not for the PANX1(ΔNTH/ΔCTT) dataset (Extended Data Fig. 6c), strongly suggesting that CBX binds to the location. Therefore, our structural analysis has ruled out the possibility that CBX can compete with NTH for PANX1 binding, but instead supports the idea that CBX functions as a pore blocker and binds to the extracellular restriction site (W74). We were unable to unambiguously define the exact positioning of CBX for two reasons. First, the two carboxyl groups of CBX lack direct interaction with the protein and are thus flexible. Second, the density is an average of the many different poses that CBX may adopt within the extracellular entrance.

Model building, validation, and structural analysis

The cryo-EM maps of PANX1 and PANX1(ΔCTT) are of excellent quality, allowing us to model almost the entire protein. De novo model building was initially conducted using Coot[64]. Registers were guided by secondary structure prediction (Extended Data Fig. 9) using JPred[65] webserver and the bulky residues of PANX1. We were able to model most of PANX1 except for the linker connecting the intracellular helices IH1 and IH2 (residues 163–190), and the CTT (residues 374–426). For regions of the map with limited side-chain information (residues 19–26, 302–305, 316–327 and 356–373), we only modelled the residue backbone. Extra density in N255 is modelled as *N*-acetyl-D-glucosamine on the basis of biochemical analysis of the wild type and N255A mutant. Putative lipid density in the map is modelled as cholesterol, diacylglycerol, phosphatidylethanolamine and distearoyl-3-*sn*-phosphatidylethanolamine on the basis of the shape of the lipid density. However, we do not have experimental evidence to claim the exact identity of these lipid molecules. The atomic model was refined using phenix.real_space_refine and evaluated using phenix.mtriage[66].

CBX–PANX1(ΔCTT), PANX1(ΔNTH/ΔCTT) and CBX–PANX1(ΔNTH/ΔCTT) models were generated using molecular dynamics-based flexible fitting with the PAXN1 model as the input[67]. The resulting model was manually adjusted and refined using phenix real-space refinement[66]. CBX molecules were manually fitted into the centre of the extracellular entrance. We provided strong structural and functional evidence to support the proposed CBX binding site. However, the two terminal carboxyl groups of CBX do not make specific interactions with the protein, and are therefore not well-defined in the map. Models were validated using phenix.molprobity[68].

The PANX1(N255A)^{Gap} and PANX1(N255A)^{Hemi} channel models were built by docking the PANX1(WT) model into the gap junction and hemichannel map. We manually adjusted the position of IH1 and IH7 helices and mutate N255 to alanine in Coot[64]. The resulting model was subjected to phenix real-space refinement and validation[66,68].

Solvent accessible contact interface is measured using the get_area function in PyMOL[69]. Electrostatic potential was calculated using the APBS Plugin embedded in PyMOL[70]. Tunnel and size analysis were done using Caver 3.0[71]. Figures were generated using PyMOL and UCSF Chimera/ChimeraX[72,73].

Electrophysiology

Using patch-clamp analysis, whole-cell currents were measured in tsA201 cells plated on poly-L-lysine-coated (Sigma) coverslips following 1–2 days of overexpression. C-terminal GFP-tagged PANX1 constructs were used for visual identification. The only untagged mutants were ΔCTT and A33C/ΔCTT, which were co-expressed with a plasmid encoding GFP. The PANX1(ΔCTT) used in Fig. 1f and Extended Data Fig. 7 is a G380 stop codon mutation to mimic the CTT-cleaved PANX1. Both viral infection (cells infected at 5% v/v of P2 virus, incubated at 37 °C for 10–12 h and then at 30 °C with medium containing 5 mM sodium butyrate) and Lipofectamine 2000 transfection were used for overexpression. Because no differences in current amplitudes were observed between methods for PANX1 and various mutants, the data were pooled. Patch pipettes contained (in mM) 145 NaCl, 10 Hepes, 10 EGTA, pH 7.3 and the bath solution contained 160 NaCl, 10 Hepes, 3 KCl, 2 $CaCl_2$, and 1 $MgCl_2$, pH 7.4. Voltage steps of 0.25 s were imposed from −100 mV to +80 mV and membrane currents were recorded (digitized at 10 kHz and filtered at 2 kHz) using a Multiclamp 700B microamplifier (Axon Instruments) and Clampex software (v.11.0.3). CBX (Sigma) was added to the bath solution at a final concentration of 0.1 mM. Currents were analysed off-line using ClampFit (v.11.0.3). Current amplitudes were measured 5 ms at a clamp of +80 mV. CBX-sensitive currents were calculated from the difference in current amplitude in a cell measured with and without CBX. For measuring ion selectivity, whole-cell currents were measured from patch-clamped cells imposed with 2-s voltage ramps (−100 mV to +100 mV) using a AgCl reference electrode and a 3 M KCl–agar bridge. Cells were first measured in symmetrical NaCl concentrations where patch pipettes contained (in mM): 145 NaCl, 10 HEPES, 10 EGTA (pH 7.35) and the bath solution contained: 145 NaCl, 10 HEPES, 2 Ca-gluconate, 1 Mg-gluconate, pH 7.4. Sucrose was added to all bath solutions for a final osmolarity of about 325 mOsm l^{-1}. Sequential measurements were performed following superfusion with various bath solutions where NaCl was replaced with equimolar amounts of NaI, Na-gluconate, and *N*-methyl-D-glucamine chloride (NMDG-Cl). Anion permeability ratios were calculated using shifts (relative to NaCl) in the zero-current reversal potential using a modified Goldman–Hodgkin–Katz equation[74]. Liquid-junction potentials were minimal (<2 mV) and uncorrected. For Na/Cl permeability ratios, zero-current reversal potentials were measured using a reduced salt bath solution containing (in mM): 14.5 NaCl, 10 Hepes, 2 Ca-gluconate, 1 Mg-gluconate, 245 sucrose and calculated using the Goldman–Hodgkin–Katz equation. Recordings were performed at room temperature. Statistical analysis of carbenoxolone-sensitive currents was performed with Mann–Whitney test (GraphPad Prism). *P* values <0.05 were deemed significant.

Molecular dynamics simulation

The lipid bilayer molecular dynamics system with PANX1(WT) was prepared using CHARMM-GUI[75]. Specifically, the PANX1(WT) model was first oriented with respect to the membrane normal using the OPM server[76]. CHARMM-GUI was then used to build the lipid bilayer system with 1-palmitoyl-2-oleoyl-*sn*-glycero-3-phosphocholine (POPC) on both sides of the membrane. PANX1 is protonated at neutral pH. The system was then solvated with 603 TIP3P water, and neutralized with approximately 150 mM NaCl (144 Na and 165 Cl ions). The final system has a dimension of 130 Å × 130 Å × 154 Å.

CHARMM36m force field parameters were used for the simulation[77]. Initial energy minimization was performed using the steepest-descent algorithm with a F_{max} tolerance of 500 kJ mol^{-1} nm^{-1}. Position restraint was enabled for non-hydrogen atoms of the protein and phosphorus atom of POPC. The system then underwent 6 rounds of equilibration with the strength of the position restraint gradually decreased (from 4,000 kJ mol^{-1} nm^{-2} to 200 kJ mol^{-1} nm^{-2} for backbone atoms, and 2,000 kJ mol^{-1} nm^{-2} to 200 kJ mol^{-1} nm^{-2} for side-chain atoms). The temperature of the system was brought to 310 K using a Berendsen thermostat by coupling protein, POPC membrane, and solvent in NVT ensemble for the first 3 rounds of equilibration. Subsequently, NPT ensemble was launched using a Berendsen semiisotropic pressure coupling at 1 bar. The linear constraint solver (LINCS) algorithm was used to constrain the hydrogen atoms[78]. NVT and NPT equilibration simulations were carried out using 1-fs and 2-fs timesteps, respectively. The unrestraint production simulation continued from the NPT ensemble using Nose-Hoover thermostat and Parrinello–Rahman barostat. The trajectory was accumulated for 100 ns using a timestep of 2 fs. The Verlet cut-off scheme was used to generate the neighbour list (12 Å) for short-range electrostatic and van der Waals interactions. Gromacs v.2019.2 was used as the molecular dynamics engine[79]. Trajectory data were analysed using the utilities of Gromacs and visualized using PyMOL[69].

Reporting summary

Further information on research design is available in the Nature Research Reporting Summary linked to this paper.

Data availability

Cryo-EM density maps have been deposited in the Electron Microscopy Data Bank (EMDB) under accession numbers EMD-21588 (PANX1(WT)), EMD-21589 (PANX1(ΔCTT)), EMD-21590 (CBX–PANX(ΔCTT))00, EMD-21591 (PANX1(ΔNTH/ΔCTT)), EMD-21592 (CBX–PANX1(ΔNTH/ΔCTT)), EMD-21593 (PANX1(N255A)^{Hemi}), EMD-21594 (PANX1(N255A)^{Gap}), EMD-21595 (apo PANX1), EMD-21596 (Ca^{2+}–PANX1), EMD-21597 (K^{+}–PANX1) and EMD-21598 (SMA–PANX1). Structure models have been deposited in the RCSB Protein Data Bank under accession codes 6WBF (PANX1(WT)), 6WBG (PANX1(ΔCTT)), 6WBI (CBX–PANX(ΔCTT)), 6WBK (PANX1(ΔNTH/ΔCTT)), 6WBL (CBX–PANX1(ΔNTH/ΔCTT)), 6WBM (PANX1(N255A)^{Hemi}) and 6WBN (PANX1(N255A)^{Gap}).

47. Goehring, A. et al. Screening and large-scale expression of membrane proteins in mammalian cells for structural studies. *Nat. Protoc.* **9**, 2574–2585 (2014).
48. Zhou, Q. et al. Target protease specificity of the viral serpin CrmA. Analysis of five caspases. *J. Biol. Chem.* **272**, 7797–7800 (1997).
49. Denault, J.-B. & Salvesen, G. S. Expression, purification, and characterization of caspases. *Curr. Protoc. Protein Sci.* **30**, 21.13.1– 21.13.15 (2002).
50. Haley, E. et al. Expression and purification of the human lipid-sensitive cation channel TRPC3 for structural determination by single-particle cryo-electron microscopy. *J. Vis. Exp.* **143**, e58754 (2019).
51. Mastronarde, D. N. Automated electron microscope tomography using robust prediction of specimen movements. *J. Struct. Biol.* **152**, 36–51 (2005).
52. Zheng, S. Q. et al. MotionCor2: anisotropic correction of beam-induced motion for improved cryo-electron microscopy. *Nat. Methods* **14**, 331–332 (2017).
53. Zhang, K. Gctf: Real-time CTF determination and correction. *J. Struct. Biol.* **193**, 1–12 (2016).
54. Rohou, A. & Grigorieff, N. CTFFIND4: Fast and accurate defocus estimation from electron micrographs. *J. Struct. Biol.* **192**, 216–221 (2015).
55. Scheres, S. H. W. RELION: implementation of a Bayesian approach to cryo-EM structure determination. *J. Struct. Biol.* **180**, 519–530 (2012).
56. Punjani, A., Rubinstein, J. L., Fleet, D. J. & Brubaker, M. A. cryoSPARC: algorithms for rapid unsupervised cryo-EM structure determination. *Nat. Methods* **14**, 290–296 (2017).
57. Zivanov, J., Nakane, T. & Scheres, S. H. W. A Bayesian approach to beam-induced motion correction in cryo-EM single-particle analysis. *IUCrJ* **6**, 5–17 (2019).
58. Zivanov, J., Nakane, T. & Scheres, S. H. W. Estimation of high-order aberrations and anisotropic magnification from cryo-EM data sets in RELION-3.1. *IUCrJ* **7**, 253–267 (2020).
59. Seminario-Vidal, L. et al. Thrombin promotes release of ATP from lung epithelial cells through coordinated activation of Rho- and Ca^{2+}-dependent signaling pathways. *J. Biol. Chem.* **284**, 20638–20648 (2009).
60. Chiu, Y.-H., Schappe, M. S., Desai, B. N. & Bayliss, D. A. Revisiting multimodal activation and channel properties of pannexin 1. *J. Gen. Physiol.* **150**, 19–39 (2018).
61. Nielsen, B. S. et al. Pannexin 1 activation and inhibition is permeant-selective. *J. Physiol.* **598**, 361–379 (2020).
62. Dourado, M., Wong, E. & Hackos, D. H. Pannexin-1 is blocked by its C-terminus through a delocalized non-specific interaction surface. *PLoS ONE* **9**, e99596 (2014).
63. Penuela, S., Bhalla, R., Nag, K. & Laird, D. W. Glycosylation regulates pannexin intermixing and cellular localization. *Mol. Biol. Cell* **20**, 4313–4323 (2009).

64. Emsley, P. & Cowtan, K. Coot: model-building tools for molecular graphics. *Acta Crystallogr. D* **60**, 2126–2132 (2004).
65. Drozdetskiy, A., Cole, C., Procter, J. & Barton, G. J. JPred4: a protein secondary structure prediction server. *Nucleic Acids Res*. **43**, W389–W394 (2015).
66. Afonine, P. V. et al. New tools for the analysis and validation of cryo-EM maps and atomic models. *Acta Crystallogr. D* **74**, 814–840 (2018).
67. Trabuco, L. G., Villa, E., Schreiner, E., Harrison, C. B. & Schulten, K. Molecular dynamics flexible fitting: a practical guide to combine cryo-electron microscopy and X-ray crystallography. *Methods* **49**, 174–180 (2009).
68. Williams, C. J. et al. MolProbity: More and better reference data for improved all-atom structure validation. *Protein Sci*. **27**, 293–315 (2018).
69. The PyMOL Molecular Graphics System v.2.1. (Schrödinger, 2020).
70. Baker, N. A., Sept, D., Joseph, S., Holst, M. J. & McCammon, J. A. Electrostatics of nanosystems: application to microtubules and the ribosome. *Proc. Natl Acad. Sci. USA* **98**, 10037–10041 (2001).
71. Chovancova, E. et al. CAVER 3.0: a tool for the analysis of transport pathways in dynamic protein structures. *PLOS Comput. Biol*. **8**, e1002708 (2012).
72. Pettersen, E. F. et al. UCSF Chimera—a visualization system for exploratory research and analysis. *J. Comput. Chem*. **25**, 1605–1612 (2004).
73. Goddard, T. D. et al. UCSF ChimeraX: Meeting modern challenges in visualization and analysis. *Protein Sci*. **27**, 14–25 (2018).
74. Shen, M. R. et al. Differential expression of volume-regulated anion channels during cell cycle progression of human cervical cancer cells. *J. Physiol*. **529**, 385–394 (2000).
75. Jo, S., Kim, T., Iyer, V. G. & Im, W. CHARMM-GUI: a web-based graphical user interface for CHARMM. *J. Comput. Chem*. **29**, 1859–1865 (2008).
76. Lomize, M. A., Pogozheva, I. D., Joo, H., Mosberg, H. I. & Lomize, A. L. OPM database and PPM web server: resources for positioning of proteins in membranes. *Nucleic Acids Res*. **40**, D370–D376 (2012).
77. Huang, J. et al. CHARMM36m: an improved force field for folded and intrinsically disordered proteins. *Nat. Methods* **14**, 71–73 (2017).
78. Hess, B. P-LINCS: a parallel linear constraint solver for molecular simulation. *J. Chem. Theory Comput*. **4**, 116–122 (2008).
79. Abraham, M. J. et al. Gromacs: high performance molecular simulations through multi-level parallelism from laptops to supercomputers. *SoftwareX* **1–2**, 19–25 (2015).

Acknowledgements We thank B. Roth for the initial construct screening; G. Zhao and X. Meng for the support with data collection at the David Van Andel Advanced Cryo-Electron Microscopy Suite; the HPC team of VARI for computational support; and D. Nadziejka for technical editing. W.L. is supported by the National Institutes of Health (NIH) (grant R56HL144929). J.D. is supported by a McKnight Scholar Award, a Klingenstein-Simon Scholar Award, a Sloan Research Fellowship in neuroscience and the NIH (grant R01NS111031). Z.R. is supported by an American Heart Association postdoctoral fellowship (grant 20POST35120556).

Author contributions W.L. and J.D. initiated and supervised the project. Z.R. performed mutagenesis, purified PANX1, prepared and screened cryo-EM samples and performed cryo-EM data collection and processing and computational simulation. I.J.O. performed electrophysiological experiments. All authors contributed in manuscript preparation.

Competing interests The authors declare no competing interests.

Additional information
Supplementary information is available for this paper at https://doi.org/10.1038/s41586-020-2357-y.
Correspondence and requests for materials should be addressed to J.D. or W.L.
Peer review information *Nature* thanks Stephen Brohawn and the other, anonymous, reviewer(s) for their contribution to the peer review of this work.
Reprints and permissions information is available at http://www.nature.com/reprints.

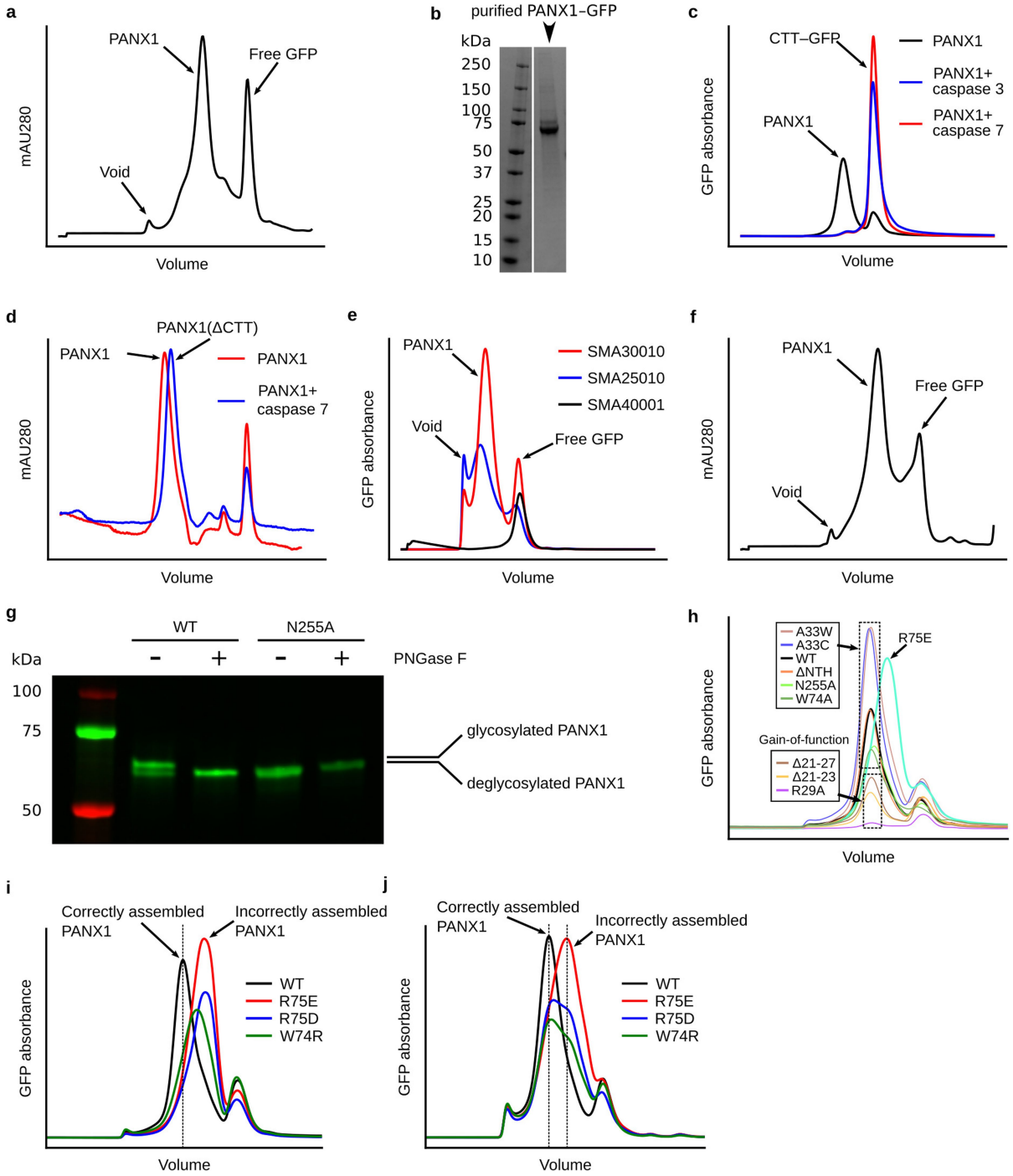

Extended Data Fig. 1 | Purification and biochemical analysis of PANX1. **a**, SEC profile of PANX1 purification using GDN. **b**, SDS–PAGE of purified PANX1–GFP. For gel source data, see Supplementary Fig. 1a. **c**, FSEC experiment for caspase 3/7 cleavage of PANX1–GFP. GFP absorbance (480 nm) is shown on the *y*-axis. **d**, Caspase 7 cleavage of purified PANX1–GFP. Cleavage of CTT results in a peak shift. Tryptophan absorbance (280 nm) is shown on the *y*-axis. **e**, SMA solubilization screening of PANX1–GFP using FSEC. Three SMA polymers (SMA25010, SMA30010 and SMA40001) were tested. GFP absorbance (480 nm) is shown on the *y*-axis. **f**, SEC profile of PANX1 purification using SMA30010. Tryptophan absorbance (280 nm) is shown on the *y*-axis. **g**, Deglycosylation test of PANX1–GFP and PANX1(N255A)–GFP using PNGase F. Bands corresponding to the glycosylated and non-glycosylated PANX1 are indicated. See Supplementary Fig. 1b for gel source data. **h**, FSEC analysis of the PANX1 mutations used for electrophysiology recordings. Cells expressing PANX1(WT) or mutants were solubilized using GDN. Gain-of-function mutations with lower expression level are labelled. The R75E mutant contains a peak position shifted to the right. **i**, **j**, FSEC analysis on extracellular-gate mutations of PANX1 solubilized using GDN (**i**) or SMA30010 (**j**). Peak positions of correctly assembled PANX1 and incorrectly assembled PANX1 are indicated by arrows and vertical bars. The W74R, R75D and R75E mutants showed decreased stability relative to wild type because, when extracted using detergent, they mostly ran at positions representing incorrect assemblies (**i**). Nevertheless, the SMA-extracted W74R, R75D and R75E mutants still showed peaks at positions representing correct assemblies (**j**), indicating that they are able to form correctly assembled channel complex in a native lipid environment.

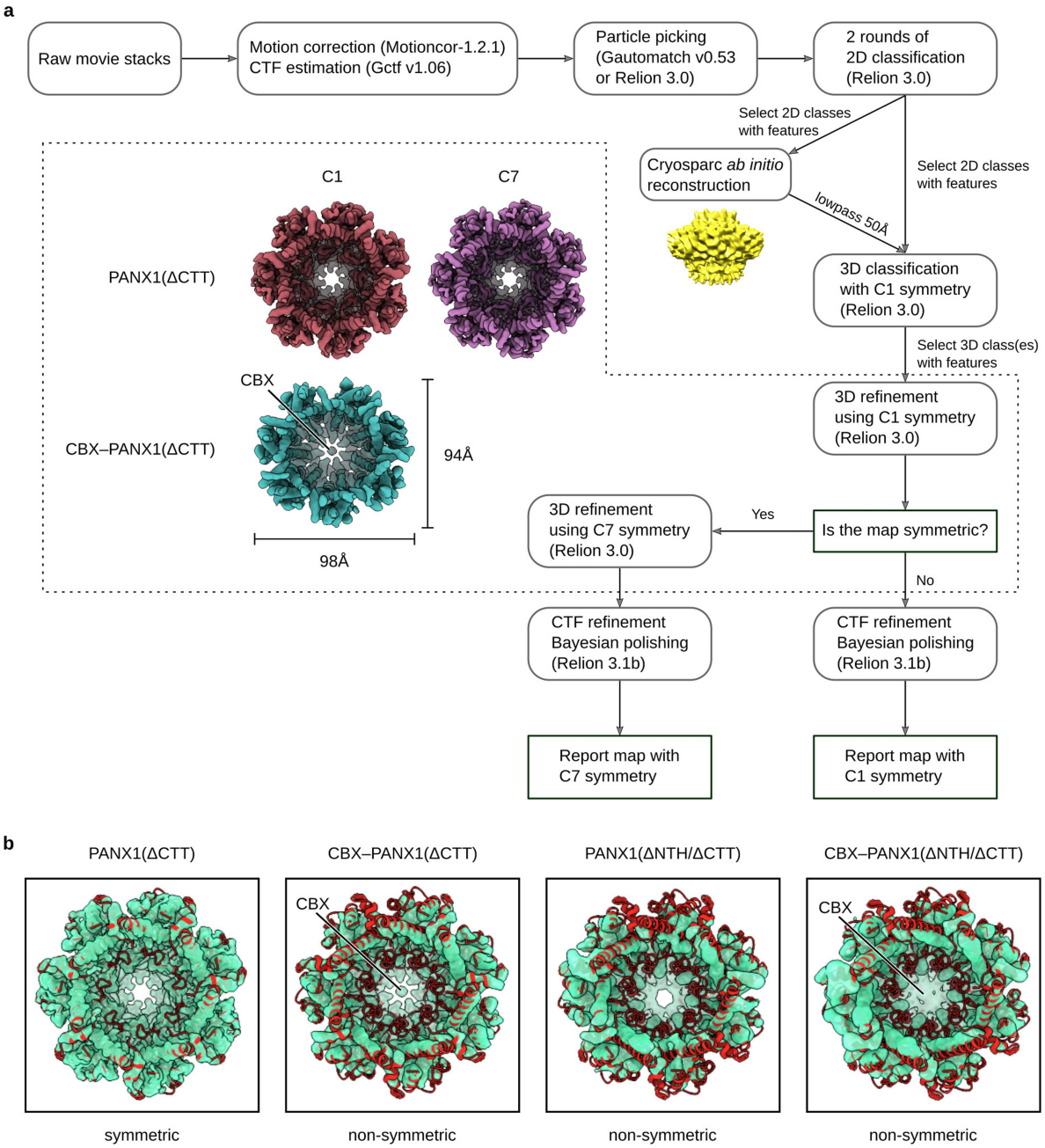

Extended Data Fig. 2 | The workflow of cryo-EM data processing of PANX1 constructs that do not form gap junctions. a, The data-analysis pipeline for PANX1 cryo-EM analysis with no gap junction. Special attention was paid to determine whether the dataset indeed adheres to C7 symmetry. Two examples of PANX1 adopting a symmetric conformation (PANX1(ΔCTT)) or a non-symmetric conformation (CBX–PANX1(ΔCTT)) are shown. A detailed description of the data-analysis procedure can be found in Methods. **b**, The overlay of the C1 refined maps of PANX1(ΔCTT), CBX–PANX1(ΔCTT), PANX1(ΔNTH/ΔCTT) and CBX–PANX1(ΔNTH/ΔCTT) with the symmetric model of PANX1. The CBX–PANX1(ΔCTT), PANX1((ΔNTH/ΔCTT)) and CBX–PANX1(ΔNTH/ΔCTT) maps adopt a non-symmetric shape.

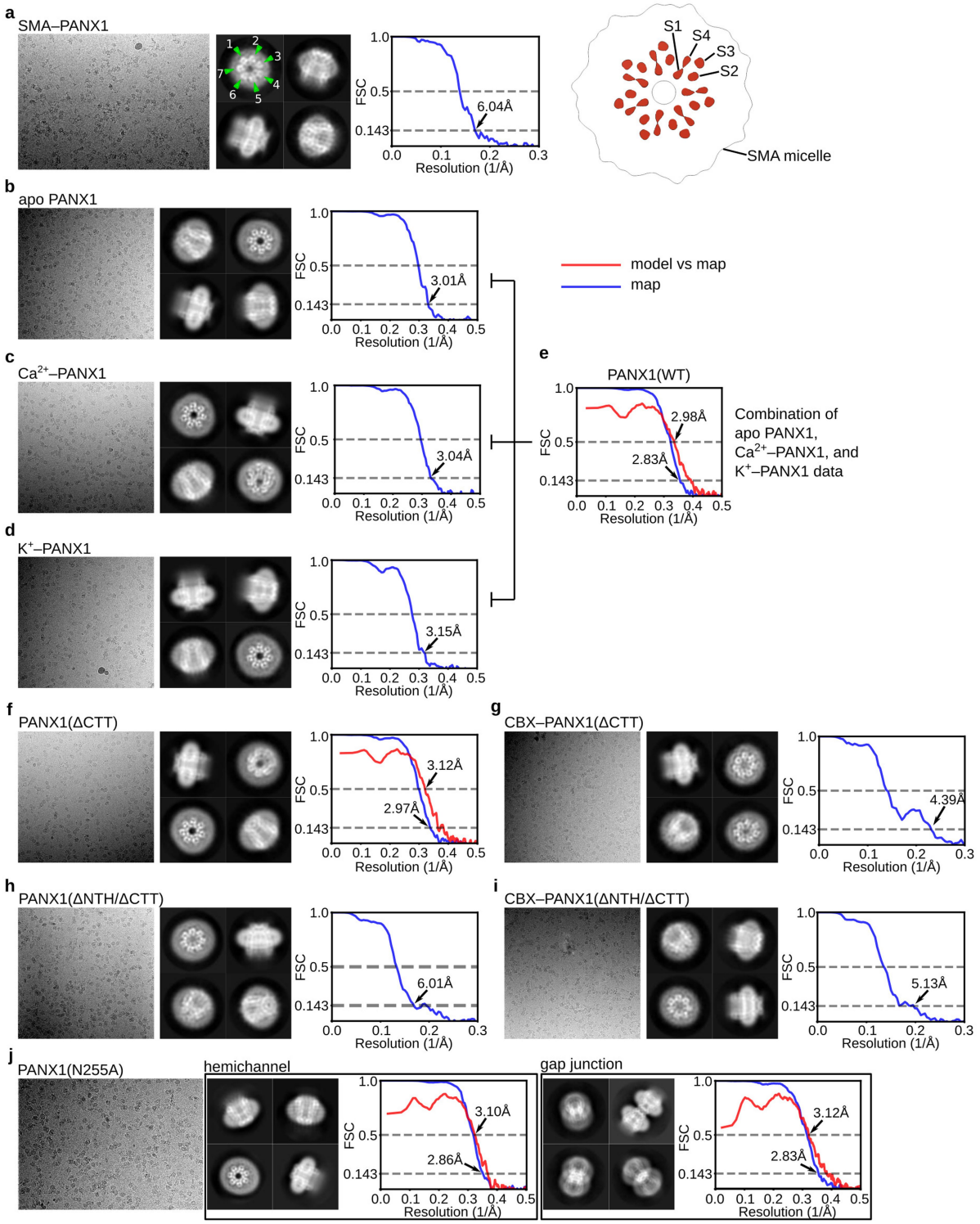

Extended Data Fig. 3 | Representative micrographs, 2D class averages and Fourier shell correlation curves for all datasets in this study. a–j, For each dataset, a representative micrograph, four 2D class averages and Fourier shell correlation (FSC) curve plot are shown, except for PANX1(N255A) dataset, in which two structures are shown. The map resolution is determined on the basis of the gold-standard 0.143 criterion. If an atomic model is available for the dataset, a model versus map FSC curve is also provided. The model versus map resolution is determined on the basis of the 0.5 FSC criterion. In **a**, a slice view of the SMA–PANX1 map showing the organization of the TMD is shown.

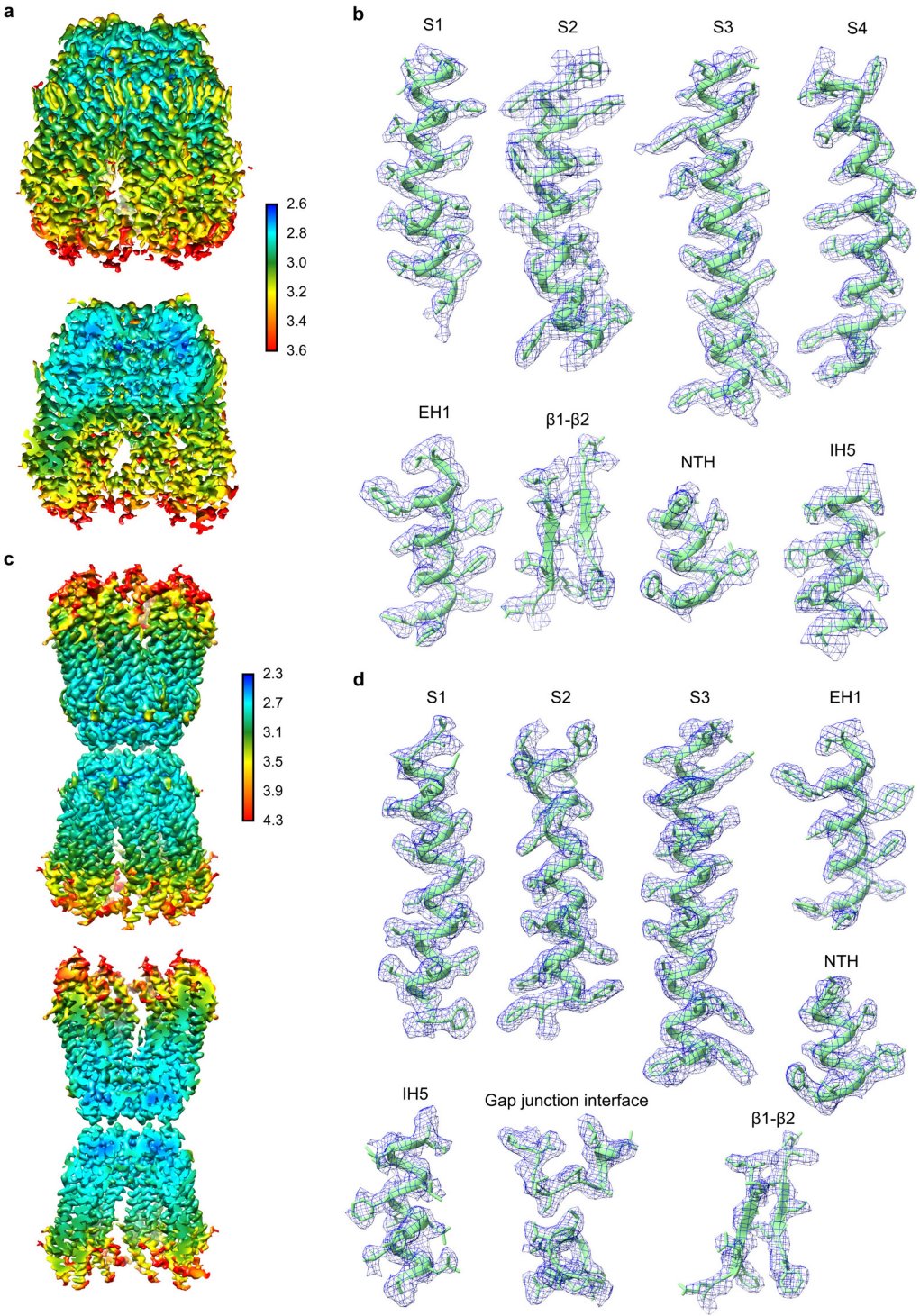

Extended Data Fig. 4 | Local resolution estimation and representative densities. a, **b**, PANX1 map. **c**, **d**, The PANX1(N255A)^{Gap} map. To provide better visualization on the exterior and interior map quality, both non-sliced and sliced views of the maps are shown. The colour represents the local resolution in Å. Representative densities are shown for a few selected secondary structure elements of PANX1.

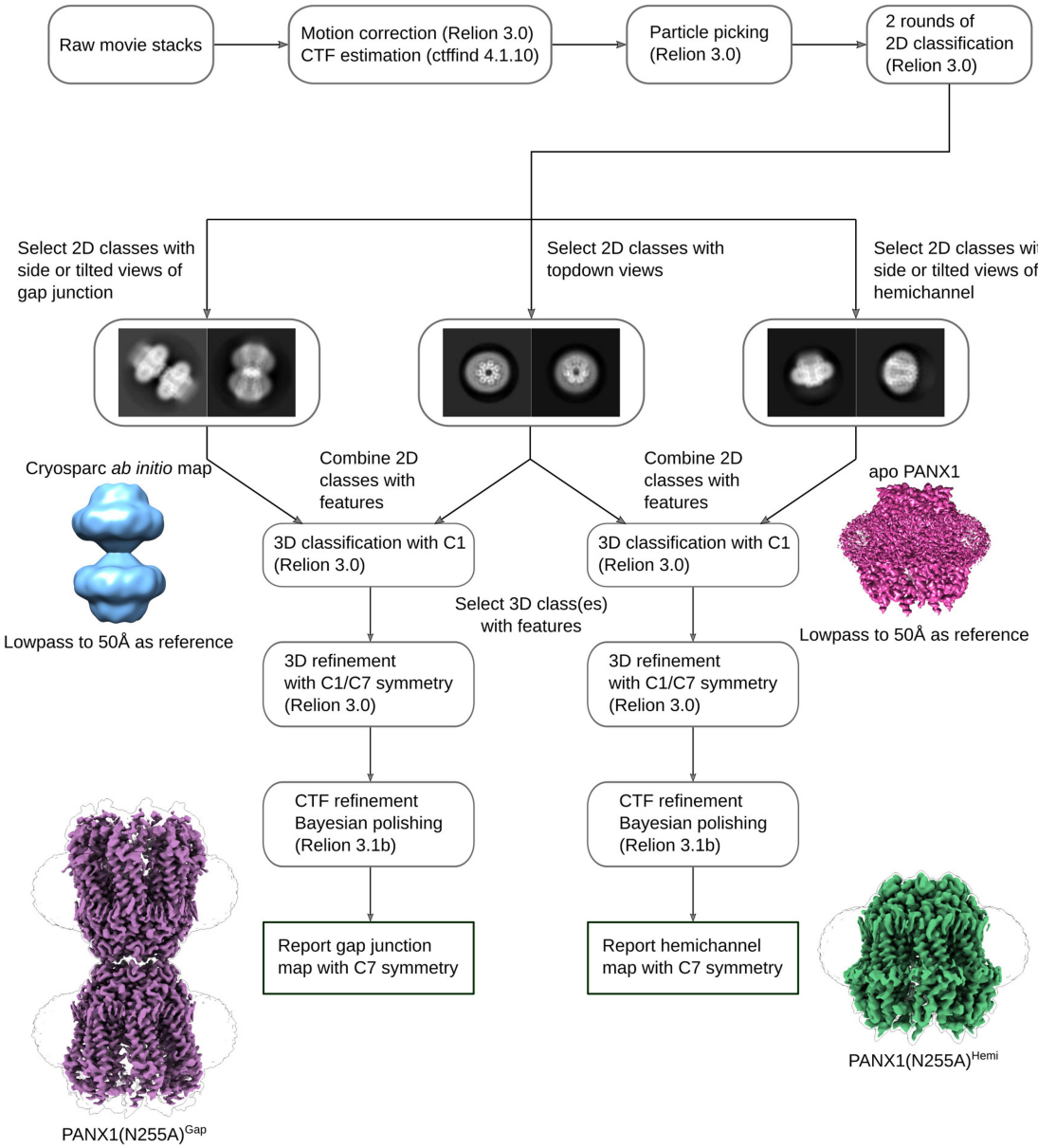

Extended Data Fig. 5 | The workflow of cryo-EM data processing for PANX1(N255A). To separate gap junction particles from hemichannel particles, we relied on 2D classification to distinguish tilted and side views. The top and down views were separated during 3D classification. A more detailed description of the data-analysis pipeline can be found in the Methods.

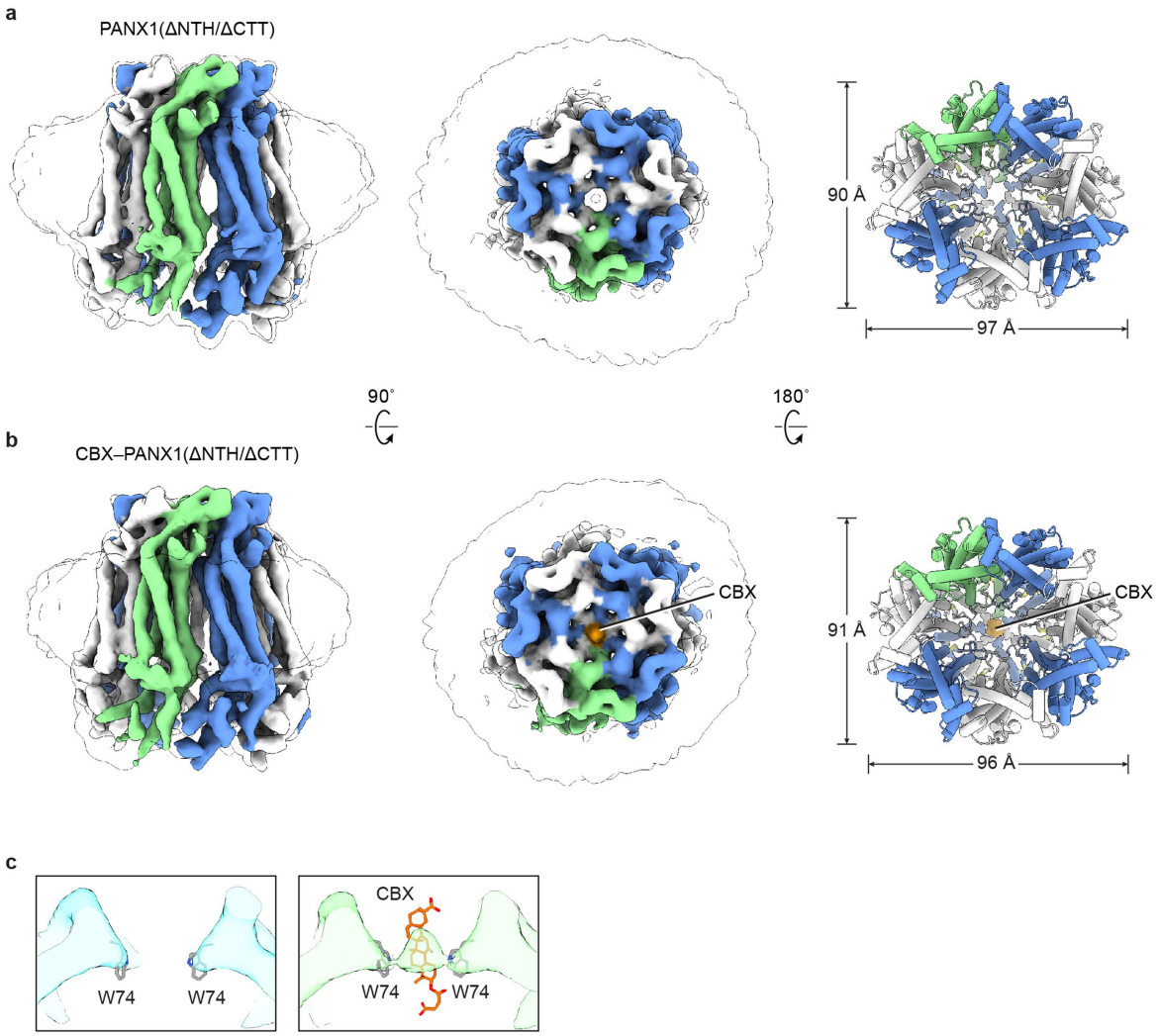

Extended Data Fig. 6 | The structures of PANX1(ΔNTH/ΔCTT). a, The apo state. **b**, PANX1(ΔNTH/ΔCTT) in complex with CBX. CBX is shown in orange. In **a**, **b**, odd- and even-numbered subunits are shown in blue and white, respectively; the seventh subunit is in green. Cryo-EM maps viewed parallel to the membrane (left) and from the extracellular side (middle). The unsharpened map is shown as a transparent envelope. Right, structural models viewed from the intracellular side. **c**, The slice view of the extracellular entrance of PANX1(ΔNTH/ΔCTT) (left) and CBX–PANX1(ΔNTH/ΔCTT) (right) maps. The CBX molecule and the side chain of W74 are shown in stick.

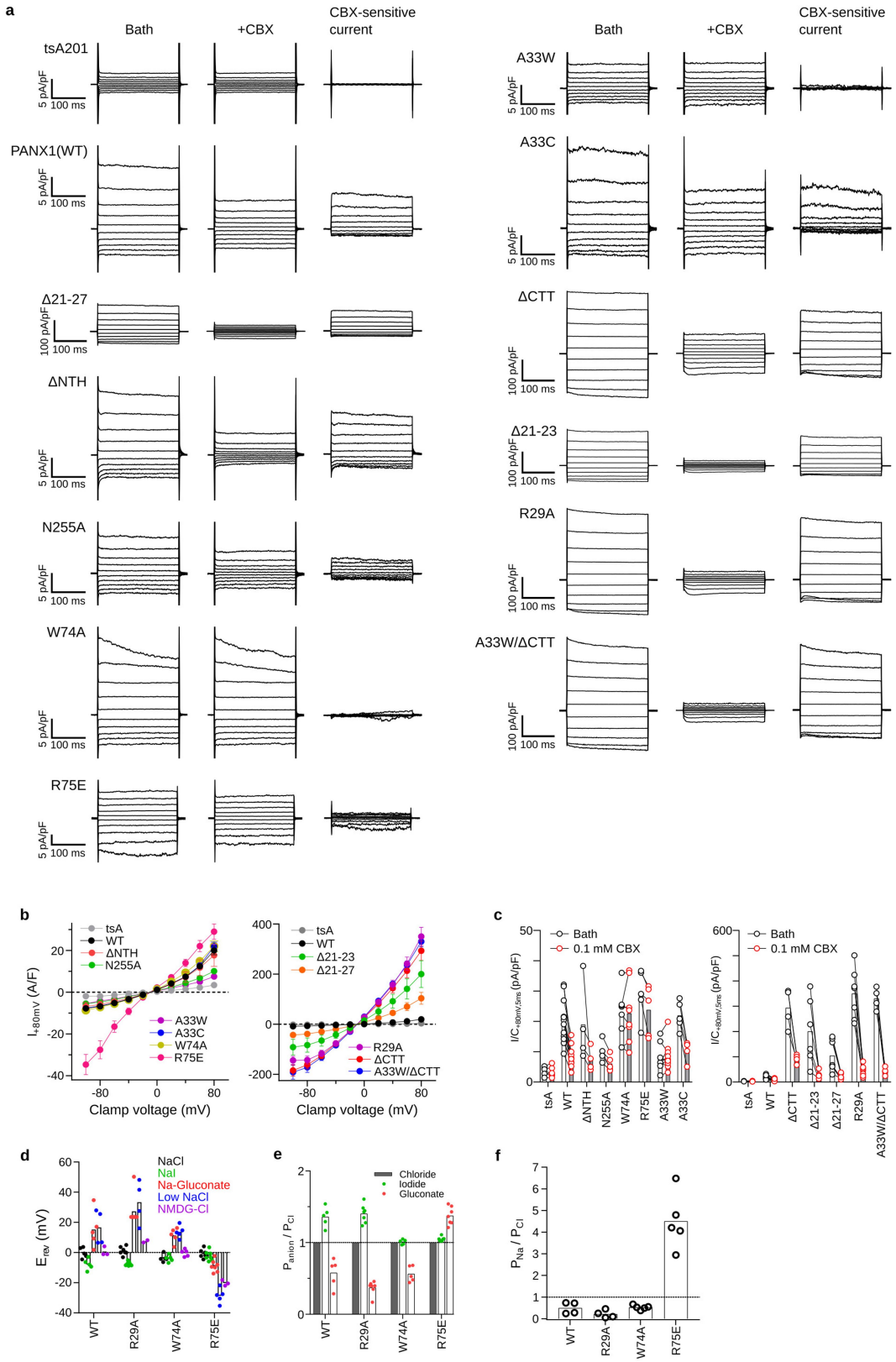

Extended Data Fig. 7 | See next page for caption.

Extended Data Fig. 7 | Patch-clamp analysis of the wild-type PANX1 and its mutants. a, Representative traces of whole-cell current density from patch-clamped tsA201 control cells ($n = 6$) and tsA201 cells overexpressing: wild type ($n = 12$) and ΔNTH ($n = 5$), W74A ($n = 8$), R75E ($n = 5$), N255A ($n = 5$), Δ21–23 ($n = 6$), Δ21–27 ($n = 7$), R29A ($n = 9$), A33W ($n = 10$), A33W/ΔCTT ($n = 4$), ΔCTT ($n = 4$) and A33C ($n = 5$) mutant PANX1. Voltage steps (0.25 s) of 20 mV were imposed from −100 mV to +80 mV from a holding potential of −10 mV. Cells were first measured in standard bath solution and then re-measured following the superfusion of a bath solution containing 0.1 mM carbenoxolone. **b**, Mean current measured at 5 ms of experiments in **a** plotted as a function of clamp voltage. **c**, Current amplitudes of experiments in **a** with and without CBX. Each paired point represents an individual cell and the bar represents the mean. **d**, Plot of zero-current reversal potentials using a 2-s voltage ramp for various bath solutions containing either (in mM): 145 NaCl, 145 NaI, 145 sodium gluconate, 14.5 NaCl or 145 NMDG-Cl (see Methods for complete solutions). The number of cells patched (indicated in parenthesis) for the various bath solutions were as follows, 145 mM NaCl: wild type (5), R29A (7), W74A (5), R75E (7); 145 mM NaI: wild type (5), R29A (7), W74A (5), R75E (7); 145 mM sodium gluconate: wild type (5), R29A (7), W74A (5), R75E (7); 14.5 mM NaCl: wild type (4), R29A (4), W74A (5), R75E (5); 145 mM NMDG-Cl: wild type (3), R29A (2), W74A (5), R75E (3). **e**, **f**, Plots of the calculated (Methods) permeability of iodide relative to chloride (P_I/P_{Cl}), the permeability of gluconate relative to chloride ($P_{gluconate}/P_{Cl}$) and permeability of sodium relative to chloride (P_{Na}/P_{Cl}) for wild-type and mutant channels. For statistical comparisons to wild type, one-way analysis of variance with Bonferroni correction was performed. For P_I/P_{Cl}, $P = 0.99$ (R29A), 3.7×10^{-5} (W74A) and 5.9×10^{-5} (R75E). For $P_{gluconate}/P_{Cl}$, $P = 0.046$ (R29A), 0.99 (W74A) and 6.8×10^{-9} (R75E). For P_{Na}/P_{Cl}, $P = 0.99$ (R29A), 0.99 (W74A) and 2.2×10^{-6} (R75E). Each point represents an individual cell. The bar represents mean and error bars show s.e.m.

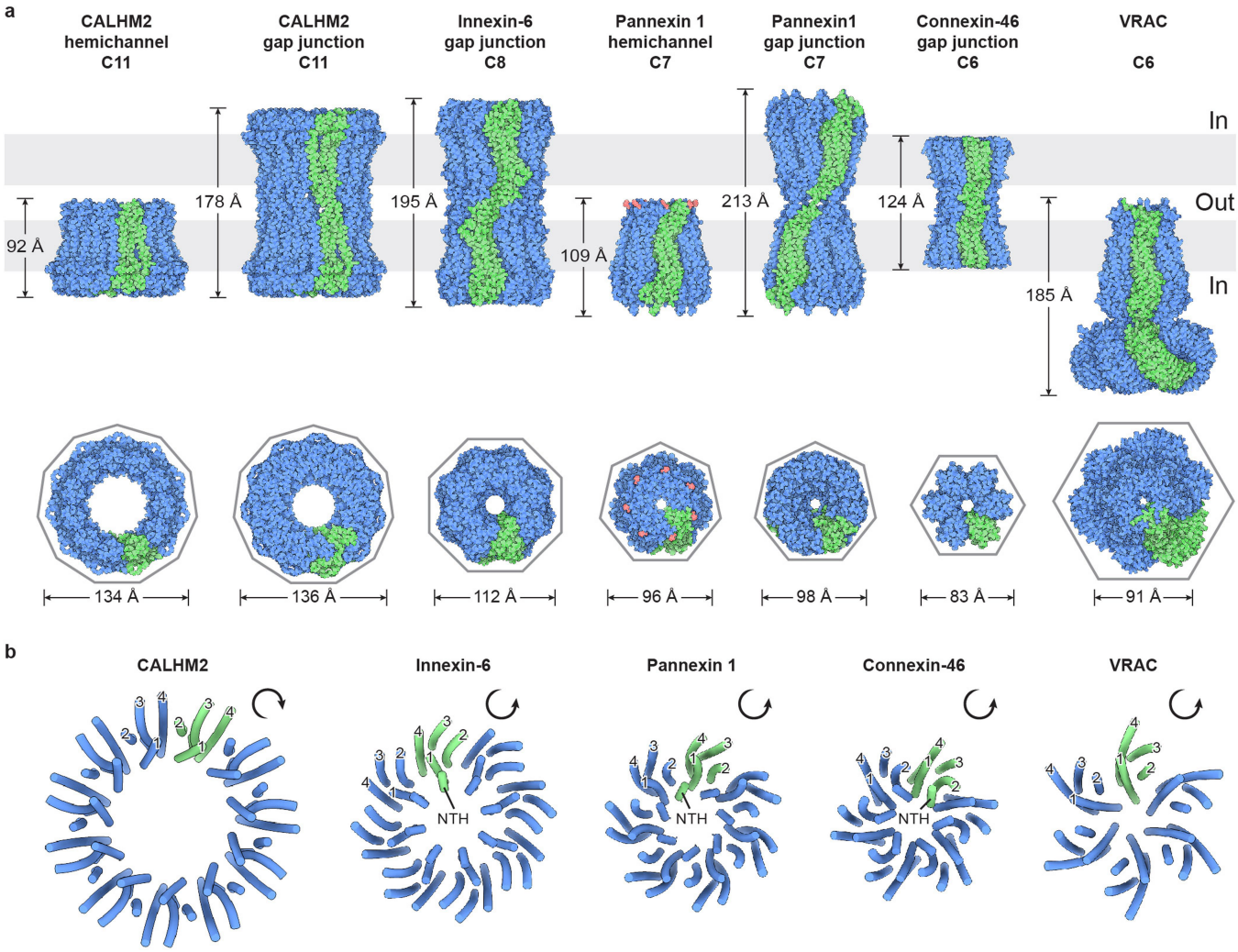

Extended Data Fig. 8 | Comparison of large-pore channels. a, The structures of large-pore channels, viewed parallel (top) or perpendicular (bottom) to the membrane. One subunit (or one pair of subunits) is in green. The diameter of VRAC is calculated without the cytoplasmic leucine-rich repeat domain. **b**, Organization of the TMD, viewed from the intracellular side. The NTH and transmembrane helices S1, S2, S3 and S4 are labelled for two subunits. Only CALHM2 has its transmembrane helices arranged in a clockwise manner. The contact between adjacent TMDs in PANX1 is made by the NTH with the S1 and S2 helices in the neighbouring subunit; the same contact in CALHM2 is made by the S2 and S4 of adjacent subunits, and in connexin by the S1 and S2 of adjacent subunits. There is no major contact in innexin and VRAC.

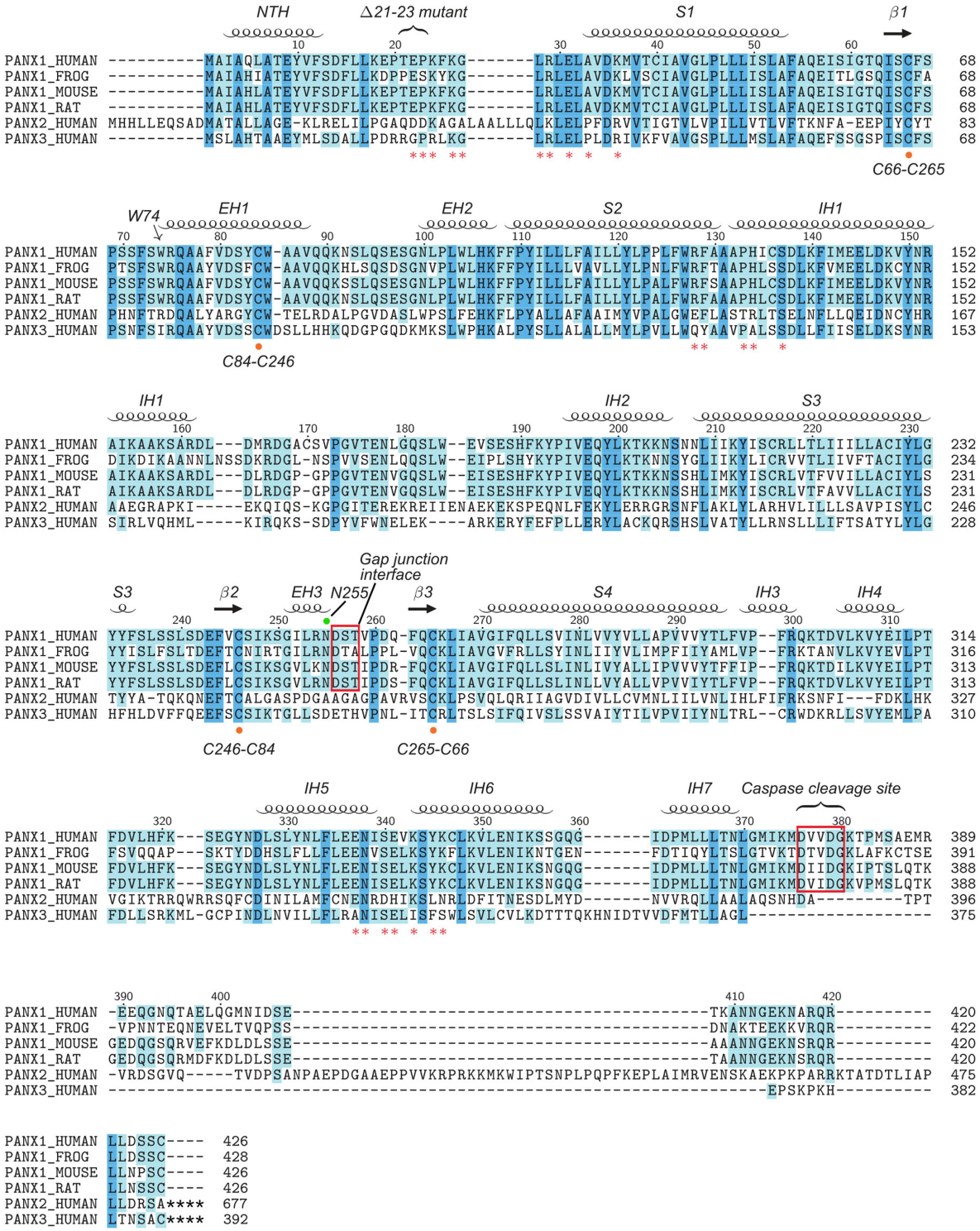

Extended Data Fig. 9 | Secondary structure arrangement and sequence alignment. Secondary structures based on the PANX1 structure model are labelled. The W74 forming the extracellular entrance is marked with an arrow. Key residues forming the side tunnel are labelled with a red asterisk. The cysteine residues forming the extracellular disulfide bonds are highlighted by an orange dot. The N255 glycosylation site is marked with a green dot. The gap junction interface and caspase 3/7 cleavage site are indicated with a red frame. A gain-of-function disease mutation (Δ21–23) of PANX1 is also marked.

Extended Data Table 1 | Cryo-EM data collection, refinement and validation statistics for PANX1(WT), apo PANX1(WT), Ca^{2+}–PANX1(WT) and K^{+}–PANX1(WT)

	PANX1(WT) (EMDB-21588) (PDB 6WBF)	apo PANX1 (EMDB-21595)	Ca^{2+}–PANX1 (EMDB-21596)	K^{+}–PANX1 (EMDB-21597)
Data collection and processing				
Magnification	130,000	130,000	130,000	130,000
Voltage (kV)	300	300	300	300
Electron exposure (e^{-}/Å^2)	49.6	49.6	49.6	49.6
Defocus range (μm)	-1.2 – -1.9	-1.2 – -1.9	-1.2 – -1.9	-1.2 – -1.9
Pixel size (Å)	1.026	1.026	1.026	1.026
Symmetry imposed	C7	C7	C7	C7
Initial particle images (no.)	1,741,195	687,650	724,686	328,859
Final particle images (no.)	179,855	87,000	74,625	45,156
Map resolution (Å)	2.83	3.01	3.04	3.15
FSC threshold	0.143	0.143	0.143	0.143
Map resolution range (Å)	2.83 – 246.2	3.01 – 246.2	3.04 – 246.2	3.15 – 246.2
Refinement				
Initial model used (PDB code)	*De novo*			
Model resolution (Å)	2.98			
FSC threshold	0.5			
Model resolution range (Å)	-103.879			
Map sharpening *B* factor (Å^2)				
Model composition				
Non-hydrogen atoms	19712			
Protein residues	2408			
Ligands	35			
R.m.s. deviations				
Bond lengths (Å)	0.005			
Bond angles (°)	0.608			
Validation				
MolProbity score	1.98			
Clashscore	13.27			
Poor rotamers (%)	0.05			
Ramachandran plot				
Favored (%)	95.65			
Allowed (%)	4.35			
Disallowed (%)	0.00			

Extended Data Table 2 | Cryo-EM data collection, refinement and validation statistics for PANX1(ΔCTT), CBX–PANX1(ΔCTT), PANX1(ΔNTH/ΔCTT) and CBX–PANX1(ΔNTH/ΔCTT)

	PANX1(ΔCTT) (EMDB-21589) (PDB 6WBG)	CBX–PANX1(ΔCTT) (EMDB-21590) (PDB 6WBI)	PANX1(ΔNTH/ΔCTT) (EMDB-21591) (PDB 6WBK)	CBX–PANX1(ΔNTH/ΔCTT) (EMDB-21592) (PDB 6WBL)
Data collection and processing				
Magnification	130,000	130,000	130,000	130,000
Voltage (kV)	300	300	300	300
Electron exposure (e^{-}/Å^2)	49.6	49.6	49.6	49.6
Defocus range (μm)	-1.2 – -1.9	-1.2 – -1.9	-1.2 – -1.9	-1.2 – -1.9
Pixel size (Å)	1.026	1.026	1.026	1.026
Symmetry imposed	C7	C1	C1	C1
Initial particle images (no.)	745,206	712,835	573,968	779,920
Final particle images (no.)	88,601	59,332	85,884	92,116
Map resolution (Å)	2.97	4.39	6.01	5.13
FSC threshold	0.143	0.143	0.143	0.143
Map resolution range (Å)	2.97 – 246.2	4.39 – 246.2	6.01 – 246.2	5.13 – 246.2
Refinement				
Initial model used (PDB code)	*De novo*	MDFF	MDFF	MDFF
Model resolution (Å)	3.12	7.04	7.17	7.17
FSC threshold	0.5	0.5	0.5	0.5
Model resolution range (Å)				
Map sharpening *B* factor (Å^2)	-97.296			
Model composition				
Non-hydrogen atoms	19712	13018	11135	11170
Protein residues	2408	2051	1948	1948
Ligands	35	1	0	1
R.m.s. deviations				
Bond lengths (Å)	0.006	0.01	0.02	0.02
Bond angles (°)	0.74	1.25	1.28	1.30
Validation				
MolProbity score	1.98	2.07	1.74	1.75
Clashscore	13.29	11.46	8.23	8.61
Poor rotamers (%)	0.38	1.2	0.00	0.00
Ramachandran plot				
Favored (%)	95.00	94.64	95.82	95.82
Allowed (%)	5.00	5.32	4.13	4.14
Disallowed (%)	0.00	0.13	0.05	0.05

Extended Data Table 3 | Cryo-EM data collection, refinement and validation statistics for PANX1(N255A)^{Hemi}, PANX1(N255A)^{Gap}, SMA–PANX1(WT)

	PANX1(N255A)^{Hemi} (EMDB-21593) (PDB 6WBM)	PANX1(N255A)^{Gap} (EMDB-21594) (PDB 6WBN)	SMA–PANX1 (EMDB-21598)
Data collection and processing			
Magnification	105,000	105,000	105,000
Voltage (kV)	300	300	300
Electron exposure (e^{-}/Å^2)	47.25	47.25	47.25
Defocus range (μm)	-1.2 – -1.8	-1.2 – -1.8	-1.2 – -1.8
Pixel size (Å)	0.812	0.812	0.812
Symmetry imposed	C7	C7	C7
Initial particle images (no.)	3,945,051	3,945,051	1,098,021
Final particle images (no.)	407,341	78,983	125,025
Map resolution (Å)	2.86	2.83	6.04
FSC threshold	0.143	0.143	0.143
Map resolution range (Å)	2.86 – 246.2	2.83 – 246.2	6.04 – 246.2
Refinement			
Initial model used (PDB code)	*De novo*	*De novo*	
Model resolution (Å)	3.10	3.12	
FSC threshold	0.5	0.5	
Model resolution range (Å)			
Map sharpening *B* factor (Å^2)	-119.822	-70.501	
Model composition			
Non-hydrogen atoms	19201	38402	
Protein residues	2387	4774	
Ligands	42	84	
R.m.s. deviations			
Bond lengths (Å)	0.006	0.01	
Bond angles (°)	0.71	1.15	
Validation			
MolProbity score	2.03	1.88	
Clashscore	13.68	11.23	
Poor rotamers (%)	0.8	0.8	
Ramachandran plot			
Favored (%)	94.40	95.51	
Allowed (%)	5.60	4.49	
Disallowed (%)	0.00	0.00	

nature research

Corresponding author(s): Wei Lü

Last updated by author(s): Mar 27, 2020

Reporting Summary

Nature Research wishes to improve the reproducibility of the work that we publish. This form provides structure for consistency and transparency in reporting. For further information on Nature Research policies, see Authors & Referees and the Editorial Policy Checklist.

Statistics

For all statistical analyses, confirm that the following items are present in the figure legend, table legend, main text, or Methods section.

n/a	Confirmed
☐	☒ The exact sample size (*n*) for each experimental group/condition, given as a discrete number and unit of measurement
☐	☒ A statement on whether measurements were taken from distinct samples or whether the same sample was measured repeatedly
☐	☒ The statistical test(s) used AND whether they are one- or two-sided *Only common tests should be described solely by name; describe more complex techniques in the Methods section.*
☒	☐ A description of all covariates tested
☐	☒ A description of any assumptions or corrections, such as tests of normality and adjustment for multiple comparisons
☐	☒ A full description of the statistical parameters including central tendency (e.g. means) or other basic estimates (e.g. regression coefficient) AND variation (e.g. standard deviation) or associated estimates of uncertainty (e.g. confidence intervals)
☐	☒ For null hypothesis testing, the test statistic (e.g. *F*, *t*, *r*) with confidence intervals, effect sizes, degrees of freedom and *P* value noted *Give P values as exact values whenever suitable.*
☒	☐ For Bayesian analysis, information on the choice of priors and Markov chain Monte Carlo settings
☒	☐ For hierarchical and complex designs, identification of the appropriate level for tests and full reporting of outcomes
☒	☐ Estimates of effect sizes (e.g. Cohen's *d*, Pearson's *r*), indicating how they were calculated

Our web collection on statistics for biologists contains articles on many of the points above.

Software and code

Policy information about availability of computer code

Data collection	SerialEM 3.7, ClampFit 11.0.3
Data analysis	Gctf-1.06, ctffind-4.1.10, Gautomatch-0.56, Relion-3.0, CryoSparc-v2, coot-0.8.9.2, pymol-2.3.2, Motioncor2-1.1.0, phenix.real_space_refine_dev_3500, phenix.molprobity_dev_3500, UCSF chimera_1.13.1, UCSF chimeraX_0.91, GraphPad Prism 7, Clampex_11.0.3, ClampFit_11.0.3, GROMACS version 2019.2, OPM server (https://opm.phar.umich.edu/ppm_server), CHARMM-GUI (http://www.charmm-gui.org/)

For manuscripts utilizing custom algorithms or software that are central to the research but not yet described in published literature, software must be made available to editors/reviewers. We strongly encourage code deposition in a community repository (e.g. GitHub). See the Nature Research guidelines for submitting code & software for further information.

Data

Policy information about availability of data

All manuscripts must include a data availability statement. This statement should provide the following information, where applicable:

- Accession codes, unique identifiers, or web links for publicly available datasets
- A list of figures that have associated raw data
- A description of any restrictions on data availability

Cryo-EM density maps have been deposited in the Electron Microscopy Data Bank (EMDB) under accession numbers EMD-21588 (PANX1(WT)), EMD-21589 (PANX1(ΔCTT)), EMD-21590 (CBX–PANX(ΔCTT))00, EMD-21591 (PANX1(ΔNTH/ΔCTT)), EMD-21592 (CBX–PANX1(ΔNTH/ΔCTT)), EMD-21593 (PANX1(N255A)Hemi), EMD-21594 (PANX1(N255A)Gap), EMD-21595 (apo PANX1), EMD-21596 (Ca2+–PANX1), EMD-21597 (K+–PANX1) and EMD-21598 (SMA–PANX1). Structure models have been deposited in the RCSB Protein Data Bank under accession codes 6WBF (PANX1(WT)), 6WBG (PANX1(ΔCTT)), 6WBI (CBX–PANX(ΔCTT)), 6WBK (PANX1(ΔNTH/ΔCTT)), 6WBL (CBX–PANX1(ΔNTH/ΔCTT)), 6WBM (PANX1(N255A)Hemi) and 6WBN (PANX1(N255A)Gap).

Field-specific reporting

Please select the one below that is the best fit for your research. If you are not sure, read the appropriate sections before making your selection.

☒ Life sciences ☐ Behavioural & social sciences ☐ Ecological, evolutionary & environmental sciences

For a reference copy of the document with all sections, see nature.com/documents/nr-reporting-summary-flat.pdf

Life sciences study design

All studies must disclose on these points even when the disclosure is negative.

Sample size	The gain of function mutations in this study showed much larger current (>10 fold) compared to wild type so that 4-6 measurements were needed. For evaluating the loss of function A33W mutant channel, sample size was increased to 10 to confirm the small differences relative to wild type. Overall, the samples sizes were deemed sufficient based on the clearly visible effects of the mutations on the mean current and the overall distribution of data points within and between each group. The sample sizes in this study are comparable to other studies characterizing various Pannexin 1 mutations.
Data exclusions	No data was excluded from the analysis.
Replication	We have done each group of experiment with several batches of cells, different infections and with independent researchers, to ensure reproducibility within the lab. All attempts at replication were successful.
Randomization	For electrophysiology experiments, cells with GFP fluorescence (proteins were GFP-tagged) were randomly selected. Other experiments including protein expression, solubilization test, protein purification, deglycosylation assay, and cryo-EM grids preparation and data collection were repeated multiple time; each time, proteins from different random batches were used.
Blinding	The investigators were blinded to group allocation during data collection and analysis.

Reporting for specific materials, systems and methods

We require information from authors about some types of materials, experimental systems and methods used in many studies. Here, indicate whether each material, system or method listed is relevant to your study. If you are not sure if a list item applies to your research, read the appropriate section before selecting a response.

Materials & experimental systems

n/a	Involved in the study
☒	☐ Antibodies
☐	☒ Eukaryotic cell lines
☒	☐ Palaeontology
☒	☐ Animals and other organisms
☒	☐ Human research participants
☒	☐ Clinical data

Methods

n/a	Involved in the study
☒	☐ ChIP-seq
☒	☐ Flow cytometry
☒	☐ MRI-based neuroimaging

Eukaryotic cell lines

Policy information about cell lines

Cell line source(s)	Sf9 cells and tsA201 cells were purchased from ATCC
Authentication	The cells were purchased and routinely maintained in our lab. They were not authenticated experimentally for these studies.
Mycoplasma contamination	Sf9 cells and tsA201 cells were tested negative form Mycoplasma contamination
Commonly misidentified lines (See ICLAC register)	No commonly misidentified lines were used